Binder Development for Binder Jetting of Aluminum Powder

by

Solgang Im

A thesis
presented to the University of Waterloo
in fulfillment of the
thesis requirement for the degree of
Master of Applied Science
in
Mechanical and Mechatronics Engineering

Waterloo, Ontario, Canada, 2021

© Solgang Im 2021

Author’s Declaration

I hereby declare that I am the sole author of this thesis. This is a true copy of the thesis, including any required final revisions, as accepted by my examiners.

I understand that my thesis may be made electronically available to the public.

Abstract

Binder jetting (BJ) is a branch of additive manufacturing (AM) technology that uses progressive addition of powders and adhesive binders to build parts with complex geometries. Compared to the other AM methods, the BJ provides a cost-effective process with a faster printing speed, high design of freedom, and negligible residual stresses generated during the printing process. This suggests the BJ as one of the most applicable technology for many industries including automotive and aerospace in fabricating functional parts with geometries such as lattice structures or internal cooling channels. The printed parts are treated with a series of thermal processes that are required to remove the excess binders and consolidate the powders. The most important factor for the BJ is the binder selection and post-process parameter determination. A failure to understand these process parameters may result in generating a porous part. Despite the possibility of high porosity, the BJ remains attractive to industries due to the many benefits it can provide with a heat-free printing process. Hence, the BJ technology was selected as a fabrication method for this study.

Aluminum is a ductile, corrosion-resistive, light-weight material with a high electrical conductivity which are being used in many industries including the automotive and aerospace. However, the surface oxide layers surrounding the aluminum powder provided a challenge for powder metallurgy industry in promoting the sintering. These oxide layers have very high thermal stability which cannot be disturbed below the melting temperature of the aluminum powder. Therefore, the sintering mechanisms are needed to disrupt the passivating layers to allow the particle diffusions. In this thesis, the conventional powder metallurgical approaches for sintering aluminum powder were addressed. These methods often involve the modification of the alloy compositions that are typically avoided by many industries due to the required resources and time. Therefore, the focus of this work was to introduce an alternative sintering agent that can interrupt the oxide films and facilitate the consolidation of aluminum powder without a need for alloy modification. In this study, the AlSi10Mg was used as a base material and the melting properties were obtained by performing the differential scanning calorimetry (DSC) technique. The first part of the research studied the polymeric binders to identify their compatibility with the aluminum powder. The selected polymers in this research were polyvinylpyrrolidone (PVP), poly (vinyl) alcohol (PVA), polyacrylic acid (PAA), polyacrylonitrile (PAN), and polyvinylidene fluoride (PVDF). Thermogravimetric analysis (TGA) was conducted to ensure that the polymer degradation temperature is below the melting point of the AlSi10Mg. Moreover, the elemental analyses were completed for the samples fabricated with the polymeric binders to investigate possible residues left after the de-binding cycle. Based on these characterization results, the most compatible polymer for the AlSi10Mg was determined. The introduction of different sintering agents was then explored to investigate the possibility

of the surface oxide layer disruption. Metallic and oxide nanoparticles, dispersed in the selected polymeric binder and metal-organic decomposition (MOD) inks, were suggested as candidates for this research. The effect of these sintering agents was studied by investigating the sintered microstructure and compositions of the test specimens using optical and scanning electron microscopy (SEM).

The elemental analyses of the de-bound test specimens were considered to determine the polymeric binder with the lowest residue contents. Polyacrylic acid (PAA) displayed the best result, where no contribution to powder composition was observed. Hence, the PAA was selected and used as a base polymeric solution to integrate the nanoparticle into the process. Fortunately, the metal-organic decomposition inks were able to fabricate the part without the help of the binding agent.

In the porosity analysis, the polymeric binders did not outperform in achieving a high-density part. The maximum density attained with the binding agent was 95.1% with the PVP solution. Conversely, all sintering agents except for the silver MOD ink achieved a density as high as 99.9%. The sintered microstructure was studied to better understand the sintering mechanisms. The SEM equipped with the energy-dispersive X-ray spectroscopy (EDX) was used to obtain high magnification micrographs and elemental compositions at the grain boundaries. The specimen constructed with the PAA was selected as a reference material, and other sintering agents having low porosities were examined in this analysis.

Only partially disrupted oxide films were observed in the test specimens fabricated with PAA and copper oxide nanoparticles, resulting in incomplete sintering. The specimen with the aluminum oxide exhibited unusual behavior, where it promoted the sintering of the oxide films together with the neighboring oxide layer. The bonded oxide films obstructed the aluminum particles from forming sinter bonds with each other. This resulted in the formation of a brittle structure susceptible to mechanical failure. In contrast, the specimens built with the copper nanoparticle and copper MOD ink demonstrated promising results. The intergranular oxide films were reconstructed with particle agglomerates composed of copper, magnesium, titanium, aluminum, and oxygen. A completely disrupted oxide film allowed the aluminum particles to diffuse through the neighboring particles and facilitated sintering. It was concluded that the copper nanoparticle and copper MOD ink were the most effective sintering agents for the aluminum alloys considered in this study.

In future work, mechanical characterization is recommended to further investigate the influence of the sintering agents. In addition, more intensive study to develop the binder suitable for the binder jetting machine is also suggested. This study may involve performing a viscosity test and adding other elements to customize the flowability of the liquid binder. Furthermore, an in-depth study can be performed to integrate the newly introduced sintering agent into the binder jetting machine.

Acknowledgments

First and foremost, I would like to express my gratitude to my advisor, Professor Etienne Martin, for giving me endless support throughout my program. Etienne, I cannot emphasize enough how thankful I am to have you as my supervisor. The continuous guidance, valuable technical advice, and thoughtful conversations that we had made my past 2 years memorable. Thank you again for your patience and constant encouragement.

I would also like to thank my adjunct advisor, Dr. Daniel Wei, who shared his valuable knowledge and insight in understanding the TGA and DSC results. Dr. Rasim Batmaz has given me continuous support with the experimental studies and suggestions for the data analysis. He was also a very supportive friend who has been always there when I most needed life advice. I would like to show my gratitude to Dr. Waqas Muhammad for sharing his insight in analyzing the SEM images. Also, I would like to thank Apratim Chakraborty for his work on the SEM images and valuable discussions and suggestions in all aspects. He was a trustworthy teammate, but also a great friend who was dedicated to giving me continuous support and inspiration. Reza Tangestani was another good friend and teammate who offered hours of phone calls whenever I needed someone to talk and rely upon. I also want to thank Khadijeh Esmati for her work on the optical microscope images. Thank you all for your support. You all helped me to get through this program.

Last but not least, I would like to appreciate the support of my best friend, Kenneth Cheong, and my family for their unconditional love and encouragement. Without your dedication and love, completing this program would have been difficult.

Table of Contents

List of Figures

List of Tables

List of Abbreviation

AM	Additive Manufacturing
ASTM	American Society for Testing and Materials
BJ	Binder Jetting
DSC	Differential Scanning Calorimetry
DED	Direct Energy Deposition
DS	Double Smoothing
EDX	Energy Dispersive X-ray Spectroscopy
FEG	Field Emission Gun
HDPE	High-density Polyethylene
HIP	Hot Isostatic Pressing
ISO	International organization for Standardization
LPS	Liquid Phase Sintering
LDPE	Low-density Polyethylene
MSDS	Material Safety Data Sheet
MIT	Massachusetts Institute of Technology
MOD	Metal-Organic Decomposition Ink
MIM	Metal Injection Molding
PAA	Polyacrylic Acid
PAN	Polyacrylonitrile
PVA	Polyvinylidene Fluoride
PVP	Polyvinylpyrrolidone
PBF	Powder Bed Fusion
PM	Powder Metallurgy
PIM	Powder Injection Molding
SSS	Solid State Sintering
TGA	Thermogravimetric Analysis
3DP	Three-dimensional Printing
UTS	Ultimate Tensile Strength
UV	Ultraviolet

1.0 Introduction

Additive Manufacturing (AM) is a technology that builds 3-dimensional (3D) objects by adding the materials layer upon layer to obtain the desired geometry. This technology offers the benefit of constructing an object that has complex geometries such as internal cooling channels or internal lattice structures. The additive method allows fabrication of the objects without a need to prepare customized molds or dies. Therefore, many industries like automotive or aerospace have gained an interest in integrating AM into their processes. The currently available AM technology is defined into seven categories based on their fusing techniques. Among these categories, binder jetting (BJ) is known as a highly flexible technique that processes powdered materials by creating an adhesion using the liquid binder. This printing process is followed by a sequence of post-processing requirements such as curing, de-powdering, de-binding, sintering, and annealing to consolidate the powders. During this consolidation process, there is a possibility of creating a substantial number of porosities. Despite this disadvantage, there is a growing interest in the BJ technology because of the benefits it offers with the heat-free printing process. This room-temperature printing process allows high design of freedom since this process is not affected by the residual stresses and related design restrictions. In addition, it also offers cheaper printing prices with a faster printing speed. However, there is limited research available regarding the BJ technology, especially in processing aluminum alloys. Hence, the application of the BJ and preliminary study of the binder system tailored for the aluminum alloys are studied in this thesis.

Aluminum is one of the most popular materials that are being used in many industries to produce a functional part. The light-weighted property of this material has attracted many fields of manufacturing including the automotive and aerospace industries to reduce the overall weight of their products. During the powder atomization process, aluminum particles react with the oxidizing agents to form aluminum oxide, resulting in the aluminum particles being covered with the oxide layer. These passivating surface layer can be beneficial during the transportation process, but it often has a negative impact in promoting the sintering. This is because of the high thermal stability of the oxide layer that cannot be thermally disturbed below the melting point of the aluminum. In order to process the aluminum alloys in the powder metallurgy industry, the alloy compositions are often modified to promote the sintering by encouraging the disruption of the oxide film. However, this process often requires extensive study and resources that most industries are hesitant to commit. Therefore, this thesis is dedicated to suggests an alternative approach that can facilitate the disruption of these passivating oxide films by modifying the binder compositions.

The focus of the current study is limited to identify 1) the compatible polymeric binding agent that has the lowest contribution to the powder composition after the de-binding cycle, and 2) the most effective sintering agent that can facilitate the disruption of the passivating surface layer. In the following chapters, the state-of-art of the BJ, existing literatures regarding the post-processing steps, and studies of conventional sintering mechanisms for aluminum alloys will be presented.

2.0 Background

Additive Manufacturing (AM) involves a progressive addition of material layer by layer to produce the part from the digital representation. This versatile technology poses a great potential to fabricate geometrically complex, value-added, and customer-specific products [1]. Ford and Despeisse identified the potential advantages of using AM technology in terms of sustainability [2]. These advantages include the (1) reduction of waste through integrating additive process instead of using subtractive process, (2) production of light-weight part to optimize the material usage and energy consumption rate, and (3) supply chain and inventory space minimization by manufacturing consumer-ready products [2]-[4]. Although there are clear benefits of using AM, there are also challenges that need to be addressed. Ngo *et al.* addressed the possible formation of voids between the subsequent layers of materials and the creation of anisotropic microstructure due to interlayer bonding deficiencies [5]. Moreover, the build process can potentially create a defect due to a thermal gradient or insufficient understanding of the process parameters. Also, the currently available AM technologies are time-intensive and expensive, thus are not preferred for high-volume manufacturing industries [6]. The advantages and disadvantages of AM technology are summarized in Table 1 [1]-[6].

Table 1: The advantages and disadvantages of AM technologies [1]-[6]

Advantages	Challenges
• Cost-efficient process for low-volume production or customized products • Capability of manufacturing parts directly from the CAD file without production tool or mold requirements • Ability to build complex geometry parts • Significantly decreased the supply chain and inventory space by creating ready-to-use products	• Possible mechanical failure due to anisotropic and heterogeneous microstructure • Potential printing defects such as porosity, lack of interlayer bonding, and shrinkage • Cost-inefficient process for mass production • Extensive study required to design new process parameters for new material • Limited material selection • Post-processing and support structure requirement

Based on the different methods of joining materials together, the American Society for Testing and Materials (ASTM) F2792 or International Organization for Standardization (ISO) 52900 classified seven categories of the AM technology: Vat photopolymerization, powder bed fusion (PBF), binder jetting (BJ), material jetting, sheet lamination, direct energy deposition (DED), and material extrusion. Vat photopolymerization uses the ultraviolet (UV) light to cure the liquid polymer resin layer after layer [7]. Alternatively, the material filament is fed through the material extrusion or DED process to additively create the product by utilizing a heat source [8], [9]. The material jetting operates similar to the 2-Dimensional (2D) printer through dispensing droplets of photosensitive material and solidifying it using the UV light [10]. The PBF and BJ are powder-bed based methods. The PBF constructs the part by melting the powders using a laser or electron beam [11]. In contrast, the BJ is a solid-state printing process that glues the materials together by replacing the heat source with a liquid binder [12].

2.1 Introduction to Binder Jetting

A group of pioneering researchers from the Massachusetts Institute of Technology (MIT) invented the BJ, originally named 'Three-dimensional printing (3DP)' in 1993. This 3DP technology uses an inkjet printhead to selectively deposit binding liquid on powder-bed to create a part geometry. In 1994, Z Corporation was founded under the direction of a professor from MIT to develop the AM machine that incorporates the 3DP technique. Until now, this technology has been mainly used for casting molds or rapid prototyping. However, as the AM industry expands, the BJ has progressively gained importance in various fields of business, primarily because of its solid-state build process and relatively high productivity compared to other AM technologies. Using these assets, the BJ process was successfully employed for different applications. The examples of these applications will be discussed later in this chapter.

The BJ is a sintering-based method that requires a series of post-processing to obtain a final part. The typical BJ sequence is shown in Figure 1. The build cycle consists of four steps: (1) the thin layer of powder is supplied through a piston or hopper mechanism, (2) the counter-rotating roller compacts and uniformly spreads the layer of powder, (3) the inkjet printhead drops the binder on demand, and (4) the powder-bed is lowered by a defined layer thickness for the next cycle. These cycles are repeated until the complete geometry is obtained [13]. The completed part is often referred as a 'green part.'

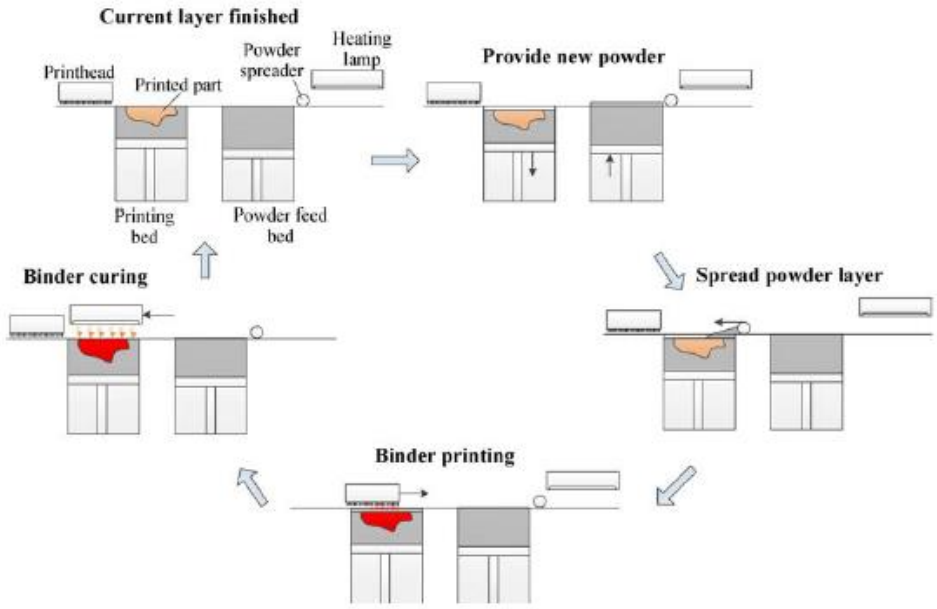

Figure 1: A schematic of the binder jetting additive process map [13]

As presented in Figure 1, the commercially available BJ machine is comprised of the following components: powder supply mechanism, spreader, printhead, build bed, and interlayer heater. The parallel powder feed system and the hopper recoater are the representative powder supply mechanisms used in the BJ process [14]. The parallel powder feed system is shown in Figure 1, where the powder is supplied by raising the powder supply tank. However, this process is not suitable for fine particle processing because it may cause the powder agglomeration. In most of the BJ processes, coarser powder is often not preferred due to its expected low-density level, hence, it was desired to develop a technology that is capable of processing fine particles. In 2017, ExOne invented the hopper recoater process to overcome the agglomerative nature of the fine particles. This invention involves a controllable vibrating powder dispenser that travels over the powder-bed to deposit a layer of powder. The application of the vibratory hopper effectively reduces the bulk strength and wall friction of the fine particles [15]. The hopper recoater can be considered as a more advanced technology that can substantially increase the flowability of the particles.

A counter-rotating (CR) roller is commonly used to spread powder on the powder-bed to improve the packing density. The vibration can be added to this conventional CR roller to facilitate spreading of the powder [16]. In 2015, Cao *et al.* presented a new approach, known as the double-smoothing (DS) method, to further improve the packing density as it reflects the quality of the final part [17]. These researchers observed a significant increase in the green density of the printed part and a noticeable decrease in internal defects. The pictorial representation of this method is illustrated in Figure 2. The DS method includes four steps: (1) the powder platform is lowered by a defined layer thickness, h, plus a thin layer of

an excess thickness, ΔH, (2) the conventional roller travels over the powder-bed and smooths the supplied powder, (3) platform is pushed upward by ΔH, and (4) the conventional roller smooths the powder-bed to remove the excess powder, leaving the defined layer thickness, h. The integration of this method can provide additional control to govern the packing behavior of the particles.

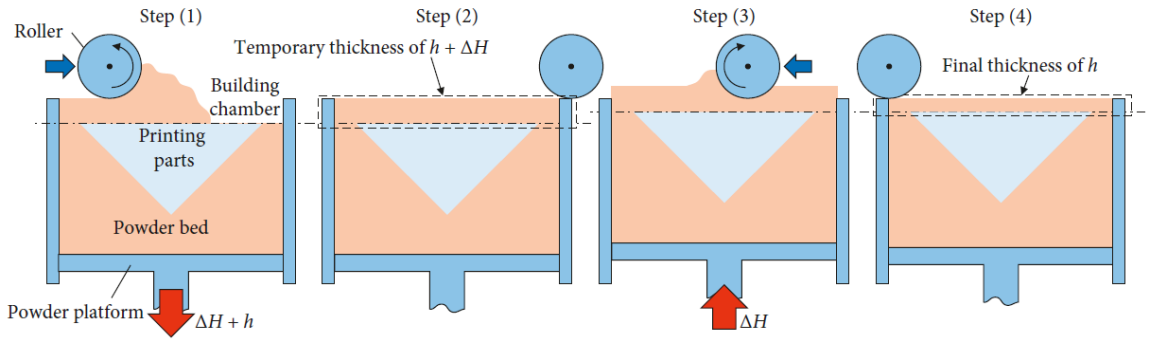

Figure 2: Double Smoothing (DS) method proposed by Cao et al. [17]

2.1.1 *Benefits and Challenges of Binder Jetting Process*

The advantages of the BJ have attracted the attention of many industries. The first advantage is the solid-state process which benefits the quality of the manufactured product in many aspects. The ability to print the green part at room temperature promotes higher design flexibility and lower residual stresses [18]. Although the green part has to be post-processed under constant heat, the processing temperature is significantly lower than the heat-involved printing method. Therefore, there is effectively no residual stress generated in the part during the BJ process in contrast to the laser or electron beam AM techniques. Hence, a complex structure such as overhangs, small features, or sharp edges can be built with minimal distortions. This heat-free build process offers higher design freedom, since the loose powders are sufficient to support the structures during the build and are not restricted by laser or electron beam design restrictions.

A wide range of material selection is another advantage of using this technology. Theoretically, this process can bind any type of material in a powder form using binding liquid. The binder formulation can be easily tailored to glue the base materials. However, prior to the production, the functionality of the binder needs to be tested and verified to ensure the quality of the final part.

The BJ process is well-known for its cost-effectiveness and ease of integration relative to other AM methods. The initial cost can be reduced significantly as the BJ process does not require high-temperature equipment (i.e. laser or electron beam) or a special atmosphere. This suggests that the BJ can be adopted easily without extensive equipment installations. In addition, the operation cost can be reduced by stacking the parts vertically in the powder-bed. The stacked parts and relatively faster printing speed can

further increase productivity, which helps to systemize the mass-production for metal AM. In the BJ process, the printing speed can be increased further without sacrificing the part quality if the process parameters are optimized for a certain product. Compared to other powder-bed AM technologies, the unbounded powders from the BJ process are highly recyclable as the powders are not heat-treated during the printing. Therefore, the BJ is recognized to be a cost-competitive option for the metal AM.

Although the BJ offers distinct benefits, there are a few processing limitations. The first disadvantage of the BJ process is a low rigidity of the green part. Before sintering, the green part can be easily damaged since the particles are held only with the adhesion. In order to achieve a desired strength and density, intensive post-processing is mandatory. However, even with a series of post-processing, it is difficult to achieve a full density part with the BJ. The typical final density of the product with an optimized process parameters ranges from 90 – 95% [19]. The required post-processing is another challenge of integrating the BJ into the operation. The green parts are densified using a process known as sintering. This process can be time-intensive and expensive to equip, particularly for industrial-scale production. Also, the binder jetted parts are prone to a network of porosity. These connected pores can be generated during the BJ process, resulting in the poor structural integrity of the final part. The post-process such as infiltration or Hot Isostatic Pressing (HIP) can be added to the post-process chain to prevent creation of the network of porosity.

The field of the BJ is still being actively studied by many researchers to reduce the porosity and increase the part density. Kumar *et al.* studied the effect of the HIP on the copper parts to evaluate density, porosity, and shrinkage of the part. The use of HIP improved the final relative density from 92% to 99.7% [20]. The study on stainless steel was also proposed by Do *et al.* to improve the process to achieve a fully dense part using the BJ [21]. Despite the challenges that the BJ faces, it is still a promising technology that offers unique benefits. Therefore, as the research expands and proceeds, there will be an expected increase in the demand and interests on the BJ industry.

2.1.2 *Current Status and Application of the Binder Jetting*

The development of the BJ technology over the past few years expanded its application to fabricating functional parts and tools from rapid prototyping [16]. Lynch *et al.* investigated the theoretical gains that can be obtained by using the BJ in the casting process compared to conventional manufacturing techniques [22]. The ability to print a complex geometry such as a cellular structure was studied by Snelling *et al*. [23]. In addition, the fabrication of injection molding tooling on the BJ is proposed by a group of researchers from MIT in 2000 [24], [25].

The BJ process is proven to outperform in manufacturing biodegradable materials compared to other AM technologies. This is possible since the amount of porosity can be controlled through manipulating the process parameters and post-process set-ups to reproduce the structure of a human bone or tissue. Hong *et al.* reported the application of the BJ to print and sinter the biodegradable Fe-Mn-Ca/Mg alloy. This study presented a successful result in terms of using micropores to achieve the desired degradation rate with good biocompatibility [26]. Furthermore, Basalah *et al.* introduced a characterization study using the BJ in the manufacturing of a titanium implant [27]. The pharmaceutical industry adopted the BJ technology to manufacture pills that can readily integrate in water [28]. This binder jetted pill was designed to help the patient who cannot take solid tablets or capsules due to the chronical health issue. Also, the ability to modify the chemical composition of the binder is an added advantage of using the BJ in the pharmaceutical industry.

Aside from the well-known applications, the BJ recently gained significant interest in the fuel-cell industry. The ability to control the porosity relative to other AM technologies draws the attention of the fuel-cell manufactures since porous anode and cathode medium determine the performance of the final product. The attempt to investigate the compatibility and performance of the BJ in fabricating a fuel-cell was studied by Manogharan *et al.* [29]. The printed part achieved a desired level of porosity and successful results were observed in the electrical discharge and permeability test.

The BJ process demonstrated its ability to fabricate different functional parts through multiple literatures. Currently, the proven process metal materials for the BJ include but are not limited to aluminum nitride [30], neodymium magnets (NdFeB) [31], stainless steels [16], [21], [32], titanium [33], [34], copper [20], [35], nickel-based superalloys [36], [37], and composite metal materials [38],[39]. The aluminum alloys are an inexpensive option for applications where both the mechanical performance and light-weighting are important. Despite of its benefits, the studies of processing aluminum alloys using the BJ have not been presented. However, as mentioned in Section 2.1, the BJ is still in a research stage which has been vigorously industrialized in many fields. Therefore, as more studies being released, there will be an indefinite potential in the BJ process for future applications [19].

2.2 Binder Jetting Post-Processing Chains

The post-processing is a mandatory step for the metal AM to achieve desired mechanical properties. The post-processing steps are binder curing, de-powdering, de-binding, and sintering. The additional post-process such as infiltration or HIP can be added to further improve the structural integrity and density of the product.

First, the powder-bed is heated after the printing process to cure the binders used to hold the particles. This binder curing stage is carried out at a relatively low temperature to polymerize the organic binder, to dry the solvent crosslink polymers, and to improve the structural integrity of the component. During the binder curing step, the green part is still surrounded by the loose powders. Once the part is cured, the powder bed is transferred to the de-powdering station. At the de-powdering station, the loose powders are removed by using a brush, air gun, or vibrating table. This is followed by de-binding, sintering, and other optional post-processes which will be discussed further in Sections 2.2.1 - 2.2.3. The processes that will be discussed in the later chapter are from the metal injection molding (MIM) industry, where the BJ technology originated from. Therefore, some techniques such as de-binding, sintering, infiltration, or HIP, that are used in the MIM industry are transferable to the BJ process.

2.2.1 *De-binding*

During the initial stage of sintering, the de-binding occurs to decompose the binder into the constituent that evaporates. The most common de-binding technique used in the BJ industry is thermal treatment. The thermal de-binding is a method where the green part is slowly heated at a constant rate until it reaches the evaporation temperature of the binder. This step is associated with evaporating and removing the binder from the system. The de-binding temperature and hold duration are the main parameters to control the process. The de-binding temperature is chosen based on the chemical composition of the binder.

The temperature selection procedures can be found in the Handbook of MIM [40]. In Figure 3, a multiple components binder system was evaluated using thermo-gravimetric analysis (TGA) [40]. The set-temperature was determined when each component was completely evaporated (see the red-dotted line). At this set-temperature, the isotherm holding time is applied to remove all binders from the part. Isothermal duration is selected based on multiple factors such as binder composition, binder quantity, and part size.

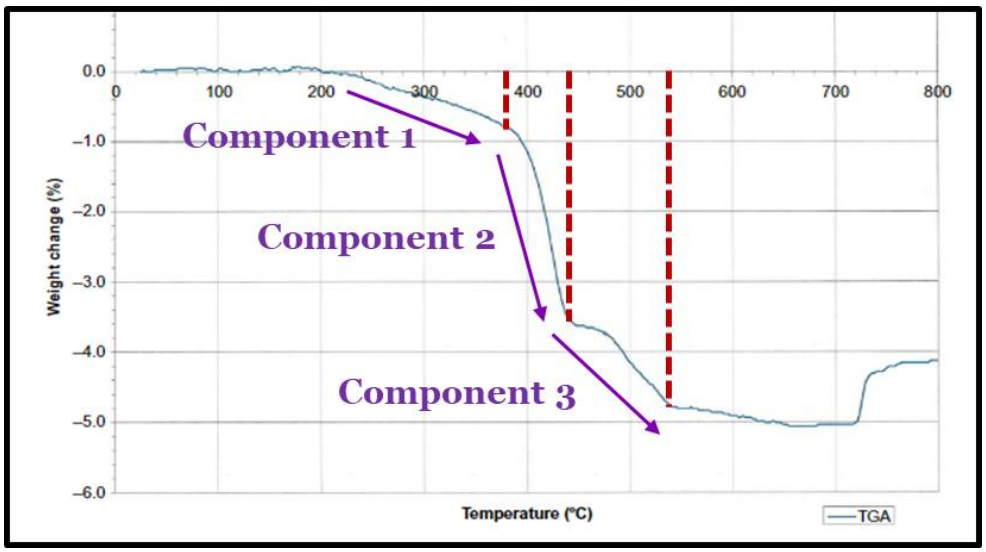

Figure 3: Thermogravimetric analysis curve for a solvent: Wax-based 4140 MIM feedstock. The de-binding temperature was determined to be: (1) component 1: 380 ℃, (2) component 2: 440℃, (3) component 3: 540 ℃ [40]

A small amount of binder remains at the final stage of de-binding (see Figure 4) to hold the powder particles until the sintering occurs to develop bonds between the particles. At this point, sintering starts to occur concurrently with the de-binding. Typically, a small sintering bonds form to hold the particles as the remained binders evaporate by the end of de-binding cycle. Formed sinter bonds retain the shape until further sintering proceeds as the temperature increases.

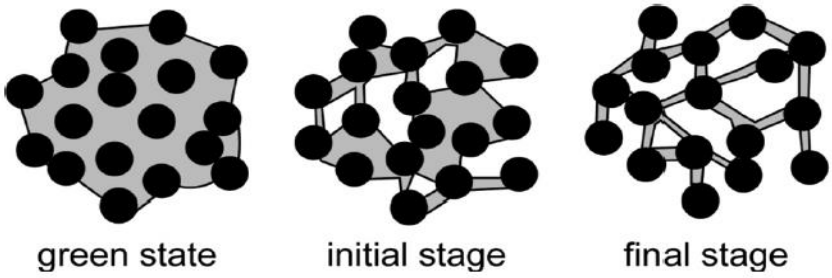

Figure 4: The visual representation of the particle structure during the de-binding process [40]

An incomplete de-binding can happen when there is remaining binder at the end of the de-binding step. The remained binder evaporates rapidly as the part is heated to the higher temperature for sintering. The incomplete de-binding can cause the part defects and soot deposition on the heating element of the furnace or inside the part. These phenomena are often a consequence of wrong de-binding temperature or insufficient holding time.

2.2.2 *Sintering*

Sintering is a process of compacting the powder to form a solid mass by applying high temperatures to fuse the particles. This process involves heating the part at a constant rate to a few degrees below the melting or solidus temperature. Sintering is associated with multiple process parameters such as sintering atmosphere, set temperature, heating rate, and holding time. A failure to understand these parameters can result in undesirable mechanical properties. The sintering atmosphere serves multiple purposes that include: (1) removal of evaporated binders at the de-binding step, (2) promotion of deoxidation to remove excess oxygen content, and (3) protection from oxidation or decarburization [40], [41]. For example, metals can be vulnerable to oxidation and decarburization during the sintering. In this case, the use of inert gas or a vacuum atmosphere often contributes to preventing the oxidation and decarburization. The effect of sintering temperature and holding time on the densification and mechanical properties of HK30 was studied by Hu *et al*. [42]. The specimen was tested for three different temperatures and holding conditions to verify the effect of each parameter on the quality of the sample. The temperature was selected 20 ℃ below and above the solidus, where the solidus temperature of HK30 is 1280 ℃. A comparison of different sintering temperatures and hold durations is summarized in Figure 5. As shown, there was a noticeable increase in the relative part density as the sintering temperature increases. In contrast, a decrease in the density was observed when the hold duration went above the threshold.

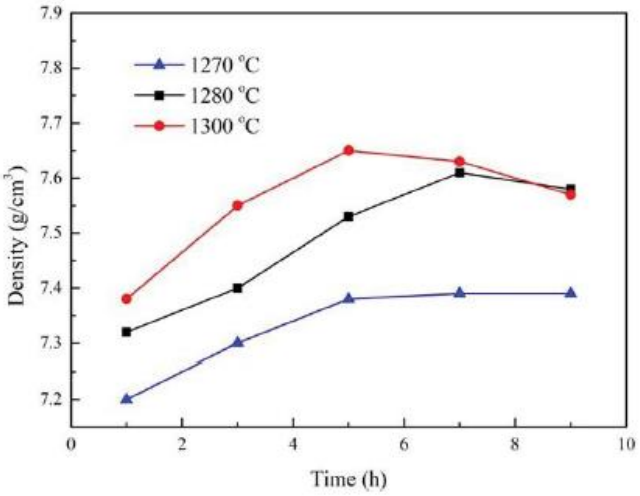

Figure 5: Density curve obtained by sintering at three temperatures and holding times [42]

A microstructure of the sintered part at a varying set temperature and hold duration was also observed in a study completed by Hu *et al*. [42]. Figure 6 illustrates the microstructure of the specimen sintered at 1300 ℃ for seven hours. A significant grain boundary coarsening and grain burns were observed. This suggests that the sintering temperature above the solidus can cause substantial damage to the part. On the other hand, Hu *et al.* also observed a microstructure of the samples at different hold duration as shown in

Figure 7. Compared to the samples sintered for five and seven hours, a specimen that was sintered for nine hours exhibited coarsened grain boundaries and damaged grains. The observations are in agreement with the density curve presented in Figure 5 which showed a decrease in density as the temperature and hold duration were increased to 1300 ℃ and nine hours, respectively. This suggests that there is a threshold for both sintering temperature and hold time to obtain optimum density. Therefore, a preliminary study is highly recommended to incorporate sintering temperature above the solidus to avoid overheating a part that can potentially degrade the mechanical property. Similarly, the hold duration threshold is also needed to be identified prior to the production for efficient process.

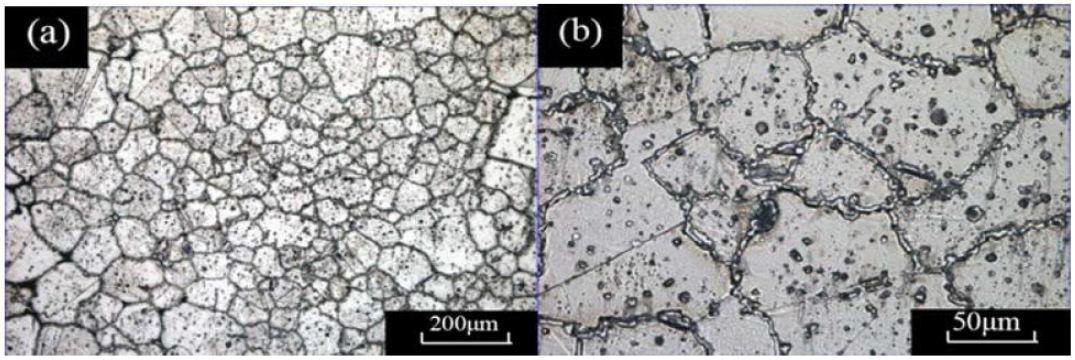

Figure 6: Microstructure of HK30 stainless steel samples sintered at 1300 ℃ for 7 hours, a) over-heated microstructure, b) over-burned microstructure with a melting zone [42]

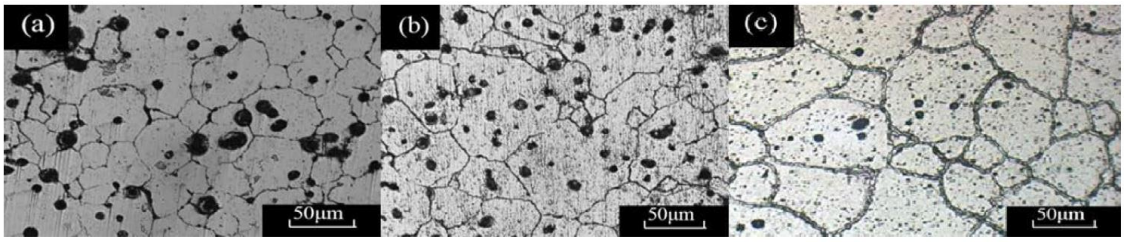

Figure 7: Microstructure of HK30 stainless steel samples sintered at 1280 ℃ for a) 5 hours, b) 7 hours, and c) 9 hours [42]

In addition to the study presented to observe the effect of sintering temperature and hold time, Coovattanachai *et al.* employed different heating rates to observe a variation in the part densification and mechanical properties. The sintered density and ultimate tensile strength (UTS) of the stainless-steel samples are summarized in Figure 8. In most of the cases, a decreasing pattern in sintered density and UTS was observed for all materials. A larger stress gradient and network of pores were observed in the samples sintered at a rapid heating rate [43]. This study suggests that the heating rate has an equivalent effect on the final property of the part as other sintering parameters. Therefore, a preliminary study is also recommended to produce a part with higher densification and structural integrity.

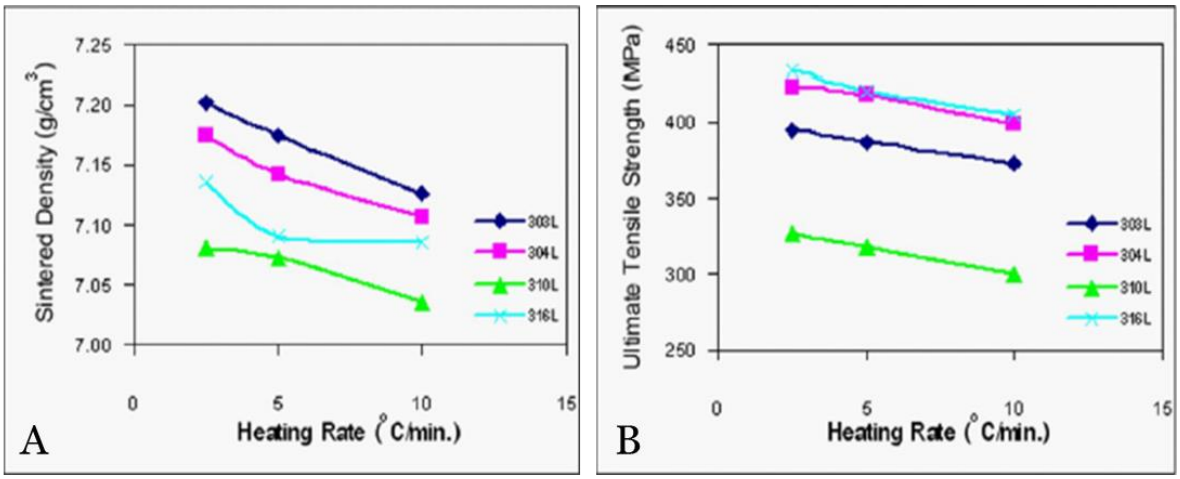

Figure 8: The sintered density curve and the ultimate tensile strength of stainless-steel specimens with varying heating rate [43]

2.2.3 *Post-sintering: Infiltration and HIP*

In Section 2.2, the mandatory post-processes are introduced which includes binder curing, de-powdering, de-binding, and sintering. In addition to these processes, there are optional operations that can be employed to improve the quality of the final part. Infiltration and HIP are the two most common additional processes which are expected to further densify the product.

The infiltration is a method to densify the part by introducing liquid material to fill the porosities. A process guide to introduce the infiltration in the BJ is studied and published by Garzon *et al.* in 2017 [44]. This preliminary study was followed by experimental work published by Cramer *et al.* in 2019 to understand the application of infiltration on the binder jetted part [45]. A tungsten carbide-cobalt is a ceramic-metal composite that is often used for the cutting tools due to its excellent hardness and fracture toughness. This material is often processed using a powder metallurgy technique, but the use of AM has been an interest as it improves the geometric complexity and throughput with no tooling costs. A pressure-less melt technique was used to infiltrate a tungsten carbide preform manufactured by the BJ with liquid cobalt for many reasons. The first reason is that a combination of the BJ and the infiltration provides a near-net shape with minimal shrinkage. This also restricts the grain growth by filling the tungsten carbide preform with the liquid cobalt. Additionally, this process effectively reduces the sintering time and temperature that is needed to sinter tungsten carbide-cobalt cermet. This method successfully achieved 98.5% relative density where the typical density of these materials on the BJ process is 92 – 94% [45].

Alternatively, the HIP is also a metallurgical process employed to improve the density and reduce the porosity of the part. This method was first invented by Battelle Memorial Institute in the 1950s and has been actively used for MIM to consolidate powders. The typical HIP process involves applying pressure

using hot compressed inert gas. In most of the cases, the temperature applied during this process is 100 – 200 ℃ below the sintering temperature [46]. Sicre-Artalejo *et al.* examined the effectiveness of the HIP process for binder jetted Inconel 718 samples [47]. All the test specimens reached full density after the HIP process regardless of their printing and sintering process parameters. Hence, the use of the HIP post-process provides a potential advantage to extend the type of powders, or binders to be used in the BJ process.

2.3 Sintering Theory

2.3.1 *Solid State Sintering*

In 1945, the first sintering model was presented by Frenkel to explain the concept of neck growth [48]. He assumed that the process consists of two identical spheres which slowly deforms into one large sphere under the influence of surface tension (see Figure 9). However, the Frenkel model ignored the crystal structure and did not consider the existence of the interparticle grain boundary and dihedral angle. Accordingly, this model was recognized for amorphous materials such as glass, but it was not used to project the sintering behavior of the crystalline materials [49]. Based on the first concept of the sintering model developed by Frenkel, Kuczynski proposed Solid State Sintering (SSS) model in 1949 [50]. In this study, Kuczynski concluded that volume diffusion was a dominant sintering mechanism for metals [51]. The controversial work was proposed by Rockland in 1967 where he suggested that grain boundary diffusion was indeed the dominant mechanism for sintering metals [52]. Since then, the Rockland model in combination with the SSS has been used to reflect the sintering behavior of the metal [19].

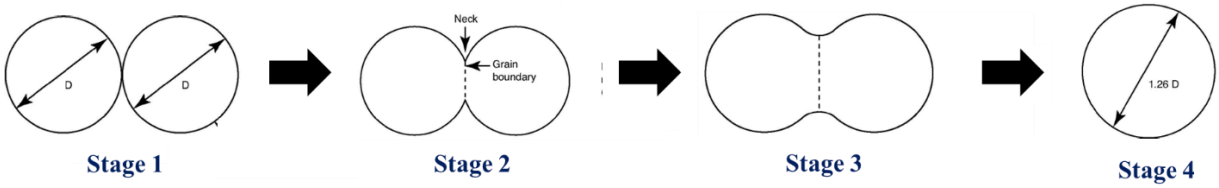

Figure 9: Two-sphere sintering model first proposed by Frenkel in 1945, which shows the neck growth until two spheres fuse into a single sphere that is 1.2 times the diameter of the starting diameter of one sphere presented in [51]

The SSS model was constructed based on the two-sphere particle model presented by Frenkel. At the beginning of the sintering process, the particles that are in contact form a system that is not thermodynamically in equilibrium (see Figure 9). This is true because the total surface energy is not at a minimum in stage 1. As sintering proceeds, the surface area decreases until the system reaches the minimum total surface energy. This phenomenon is known as sintering and the process of reducing the surface energy can be shown in Figure 9 [51].

The SSS is carried out in three stages: (1) initial stage, (2) intermediate stage, and (3) final stage [40]. The initial stage is characterized by the formation of necks between the particles. At this stage, the part density corresponds to less than 70% with the neck size smaller than one-third of particle size. The parts during the initial stage also experience lower dimensional change with less than 3% of linear shrinkage. Also, the initial stage is associated with the creation of irregular and angular pores between particles as shown in Figure 10. The intermediate stage is initiated by the neck growth where the neck size is larger than one-third of the particle size. During this stage, typical density ranges from 70-92% for spherical particles. At the intermediate stage, the pores are still interconnected to the external surfaces. The final stage occurs above 92% of relative density and is characterized by pore elimination and pore isolation [53].

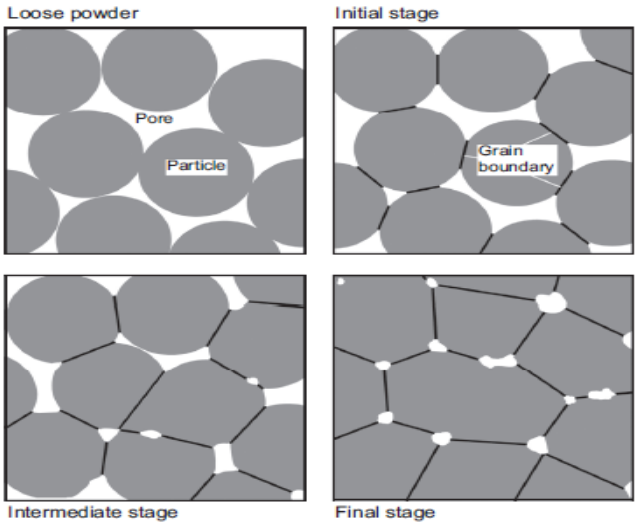

Figure 10: Graphical representation of the solid state sintering process which involves neck initiation, neck growth, and pore elimination or isolation process presented by [53]

In thermodynamic aspect, the sintering is surface energy reduction process. The surface energy of the system varies with the crystal orientations and density of the broken atomic bonds as these sites create the atomic interactions. The broken atomic bonds from different crystal lattices randomly arrange to create the grain boundary misorientations [53]. This random arrangement indicates that any grain boundary configurations are possible. The bonding efficiencies are determined by the misorientations of the grain boundary and associated energy in bonding surface [54]. Some grains rearrange their configuration to enhance the bonding by reducing the grain boundary energy [55]. During sintering, the capillary stress is also generated as the sintering progress under the influence of the surface energy. The capillary stress, σ *[Pa]*, describes the sintering bond formation as a function of surface energy, γ *[J/m^2]*, and radius of particles, R_1 and R_2 *[m]*. The bond formation between two particles with radii of R_1 *and* R_2 are represented in Equation 1 [53].

$$\sigma = \gamma\left(\frac{1}{R_1} + \frac{1}{R_2}\right) \quad (1)$$

The sintering process can be described as a mass transportation where the atomic motion is thermally stimulated. The amount of vacant atomic sites and atoms with sufficient energy to occupy those sites depends on an Arrhenius temperature relation. The Arrhenius relation is described in Equation 2, where the volume or grain diffusion coefficient, $D_V\ [m^2/s]$, is determined by the atomic vibrational frequency, $D_o\ [m^2/s]$, absolute sintering temperature, $T\ [K]$, the universal gas constant, $R\ [J{\cdot}K{\cdot}mol^{-1}]$, and the activation energy, $Q\ [J]$ [48], [53]. In the Arrhenius relation, the activation energy determines the probability of having the atoms with enough energy to relocate to the vacant sites.

$$D_v = D_0 \exp\left(-\frac{Q}{RT}\right) \quad (2)$$

The amount of mass flow during the sintering is determined by the driving force of the sintering. During the initial to the intermediate stage of the sintering, a surface transport mechanism dominates the process. The surface transport mechanism is rearrangements of atoms around the curvature gradient of joined particles without densifying the part. In the metal sintering process, surface diffusion is the most important mechanism that promotes the active relocation of atoms. As the sintering progresses, the surface diffusion slows down due to the reduction in the surface area. When the relative density of the part is between 70 – 92% [19], a bulk transport mechanism dominates the sintering process. The grain boundary diffusion is a type of the bulk transport which is the predominant sintering mechanism for metals. The defective regions in the grain boundaries have high atomic mobility which promotes active densification [54]. This process involves relocating the atoms from the surface and inside the solid to deposit it on the vacant sites. However, the active promotion of densification using the grain boundary diffusion decreases the dimensional integrity of the part since the process continually moves the atoms from the inside the particle to fill the vacancy [40], [56].

There are other sintering mechanisms such as viscous flow, volume diffusion, or plastic flow [40]. The viscous flow is the mass transport mechanism that occurs when sintering the amorphous materials. This mechanism continues until the curvature gradients between two particles are eliminated. The volume diffusion and plastic flow is another mass transport mechanism that occurs when sintering the crystalline materials. These sintering mechanisms assist in neck formation and densification by relocating the atoms through interstitial defects such as dislocations or vacancies. However, the importance of those sintering mechanisms is insignificant compared to grain boundary and surface diffusion since the effect of these sintering mechanisms are minor [40], [54].

2.3.2 *Liquid Phase Sintering*

Liquid Phase Sintering (LPS) is a consolidation technique that is mainly used to improve the density and structural integrity of the part. Moreover, the LPS can be used to lower the sintering temperature, to achieve desired grain growth, or to tailor the grain boundary properties [54]. This method involves heating the part above the solidus of the powder material in the presence of the liquid. The volume fraction of the liquid phase should be designed to range from 5 – 15% to maintain the structural integrity of the part [19]. While the SSS is more applicable to sinter the pure metals, the LPS has been a popular method to sinter the multi-material system or alloys to promote the higher densification. In general, 90% of densification happens in the SSS during heating to the LPS temperature and further densification occurs under the influence of the liquid phase [57].

The LPS is driven by the capillary force created by the pressure difference between the narrow and wide capillary channels within the solid particles. During this process, the vacant site created by the melted particles can create the pores as the liquid flows into the capillaries. The overall densification kinetics for the LPS would be the elimination of the generated pores [54]. Similar to the SSS, the pores elimination and the grain growth occur concurrently with the sintering. During the LPS, particle rearrangement can occur where the microstructural change happens by the liquid flow. The occurrence of particle rearrangement depends on the multiple factors including the volume fraction of liquid phase, dihedral angle, particle size, and isothermal hold duration at the LPS temperature. The dihedral angle can be described as the angle formed between the grain boundary and another solid, pore, or liquid. The particle rearrangement may not happen if the dihedral angle is larger than 0° [57]. The dihedral angle defines the interface between the grain boundary, solid, and liquid phases as shown in Equation 3 [54]. The solid-solid interface energy, γ_{SS} *[J/m^2]*, is described by the solid-liquid interface energy, γ_{SL} *[J/m^2]*, and dihedral angle, ϕ.

$$\gamma_{SS} = 2\gamma_{SL} cos\left(\frac{\phi}{2}\right) \tag{3}$$

During the LPS, the part consists of liquid, solid, and vapor phases. The grain growth in the presence of the liquid phase is known as the Ostwald ripening. The LPS occurs in a sequence to the SSS stages as shown in Figure 11. The LPS involves with four steps: (1) liquid phase formation and redistribution into the solids, (2) solid phase rearrangement driven by the capillary stress, (3) grain shape and density change of the solid phase involving precipitation of liquid phase, and (4) microstructural evolution dominated by Ostwald ripening which further increases the part densification [54].

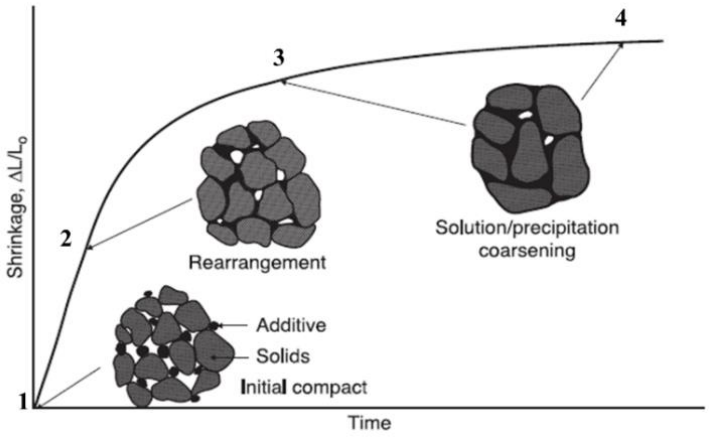

Figure 11: Pictorial representation of the microstructural evolution of a powder compact during the LPS proposed by German [54]

The wetting liquid is another important factor of the LPS [57]. The contact angle, θ, can be used to measure the wetting property. This angle forms at the intersection of liquid, solid, and vapor phases as shown in Figure 12 [54].

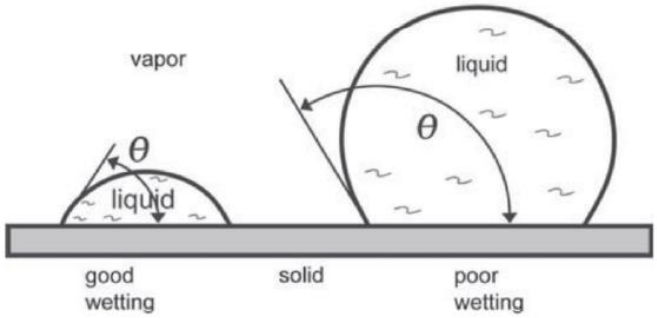

Figure 12: The wetting behavior of the liquid interface against the solid and vapor phases. Smaller contact angle promotes good wetting property which overall improves the densification [19]

The contact angle is defined by performing the equilibrium energy balance on the horizontal surfaces when the gravity is ignored. The contact angle is described in Equation 4, where γ_{SV}, γ_{SL}, and γ_{LV} are the surface energy of the solid-vapor, solid-liquid, and liquid-vapor interfaces, respectively [54].

$$\gamma_{SV} = \gamma_{SL} + \gamma_{LV}\cos(\theta) \quad (4)$$

2.4 Conventional Powder Metallurgy of Aluminum Alloys

Pure aluminum is a soft, ductile, light, and corrosion-resistive material that has a high electrical conductivity. There are numerous applications of aluminum in different fields of industrial product. Ever

since the oil shortage and enforced environmental regulations, the automotive and aerospace industry gained an interest in using aluminum to manufacture light-weighted products [58]. However, the strength of the aluminum is not substantial to fabricate a functional part for such purposes. Therefore, the alloying materials such as manganese, magnesium, silicon, or copper were added to enhance the strength and formability of aluminum. In the powder injection molding (PIM) industry, aluminum and its alloys are processed using metal injection molding (MIM) method. The powders that are used in such process are generally manufactured using air atomization. During the atomization process, aluminum particles react with the oxidizing agent in the atomization gas to form an aluminum oxide, also known as alumina or aluminum sesquioxide (Al_2O_3) [59]. This process produces particles with aluminum core coated with a thin oxide layer.

The oxide layer is beneficial during the transportation and storage of the aluminum alloys as it reduces the explosive tendency [60]. This is possible due to the thermodynamic stability of the oxide layer. In turn, these surface layers hinder the sintering process of aluminum alloys. The decomposition temperature of the oxide layer is significantly higher than the melting temperature of the aluminum. The thermal stability of the oxide layer can be disrupted at the melting temperature of the aluminum if (1) the partial pressure of oxygen is less than 10^{-50} or, (2) a dew point is less than -140 ℃ [61]. However, since these conditions are not practically achievable, the reduction mechanism of surface oxide on the aluminum particles was invented by former researchers. This mechanism involves introducing the elements that have a higher affinity to form a metal oxide to the aluminum alloys to disrupt the oxide layer. Ellingham plotted the standard Gibbs energy change of formation, ΔG_f°, as a function of varying temperature to identify the affinities of different metal components to form the metal oxide (See Figure 13). A negative ΔG_f° indicates that the reaction will proceed spontaneously without external inputs, where the positive values represent a lower affinity to form the metal oxide. The Ellingham's diagram that shows the compatible elements for disrupting the oxide layer on aluminum is shown in Figure 13. Compared to the aluminum, magnesium and calcium have lower ΔG_f° which represents the higher affinity to form the metal oxides. Based on this analysis, Lumley *et al.*[62] and Kimura *et al.*[63] investigated the reduction mechanism of the oxide layers on aluminum alloys by employing magnesium in 1997.

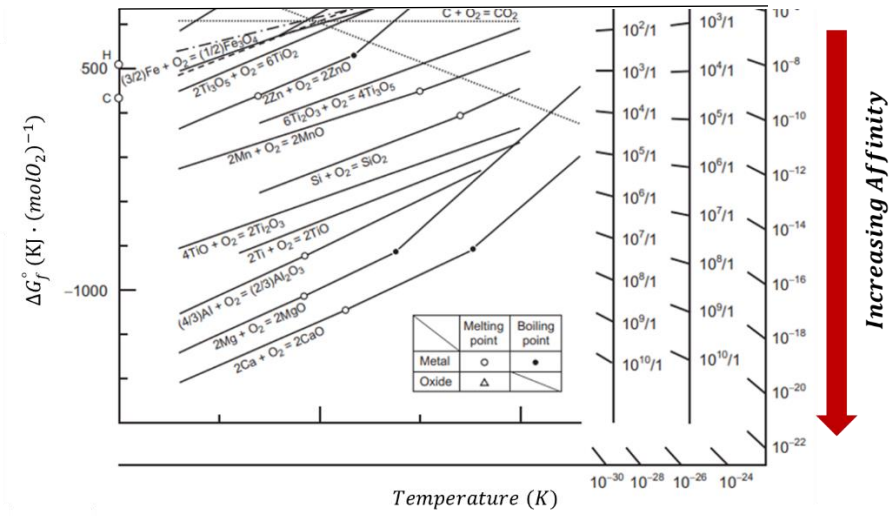

Figure 13: A fragment of the Ellingham diagram for the formation of the oxide. The full Ellingham diagram can be found in Appendix A

2.4.1 *Conventional Sintering Mechanisms of Aluminium Alloys*

The addition of magnesium is a proven powder metallurgy (PM) method to sinter aluminum to high-density. The first principle evaluation of the effect of magnesium was studied by Lumley *et al.* in 1997 [62]. Magnesium is a highly reactive element that acts as a solid-reducing agent when added to the aluminum alloys. Aforementioned, the Gibbs free energy of formation of the magnesium is lower than that of the oxide of aluminum, which allows the magnesium to reduce the alumina. This phenomenon disrupts the passivating surface layer by forming the spinel phase ($MgAl_2O_4$) at the metal-oxide interface [64]. As a result, this process facilitates the solid-state sintering, as well as the liquid-phase sintering by promoting the interactions between the particles. The adequate dispersion of the magnesium in the existence of the oxide and before the substantial liquid-phase formation is promoted by adding the magnesium in a small amount. With the small concentration of magnesium, a partial reduction reaction is favored (See Equation 5).

$$3Mg + 4Al_2O_3 \leftrightarrow 3MgAl_2O_4 + 2Al \quad (5)$$

This reaction becomes unfavored when there is magnesium concentration greater than 4 weight percent. If there is an excess amount of magnesium in the aluminum after the oxide layer has been disrupted, an expansion by the Kirkendall effect may occur [61], [62]. The occurrence of this event can degrade the sintered density and mechanical property of the final product. The optimum concentration of magnesium depends on the present oxide layer which highly fluctuates based on the particle size of the aluminum. The optimum magnesium concentration with respect to the oxide volume was evaluated by Lumley *et al.* (See Figure 14) [62].

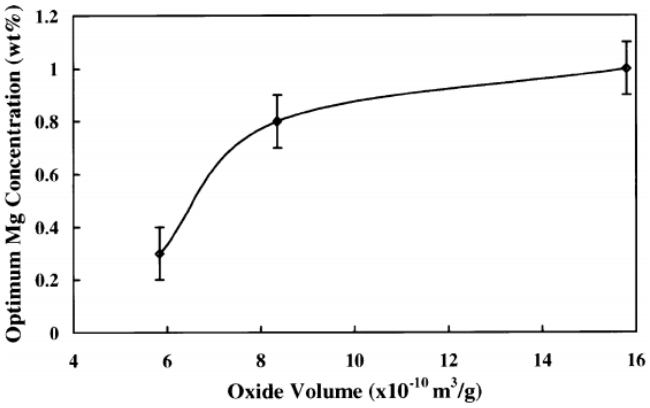

Figure 14: The optimum concentration of magnesium needed to achieve a high-density part in a binary Al-Mg alloy with respect to the present oxide volume for three different particle sizes. It clearly shows that a higher concentration of magnesium is required to sinter smaller particles due to the greater relative amount of oxide [62]

In 2010, MacAskill *et al.* studied the effect of magnesium concentrations on the sintering response of aluminum powders [60]. An elemental addition of magnesium and pre-alloyed aluminum-magnesium powders were used to investigate the significance of magnesium. The particle size of pure aluminum and pre-alloyed powders that were used in this experiment was 104 μm and 42 μm, respectively. A sintered density of the printed part with elemental and pre-alloyed magnesium added at different concentrations are shown in Figure 15. The sintered density significantly increased with the magnesium concentration less than 0.15 and 0.5 weight percent for the elemental and pre-alloyed part, respectively. The smaller particle size of the pre-alloyed part increased the available oxide layer for the reaction, which caused the system to facilitate higher magnesium concentration without degrading the physical property of the part. This noticeable increase in the sintered density deteriorated as the magnesium content increased [60].

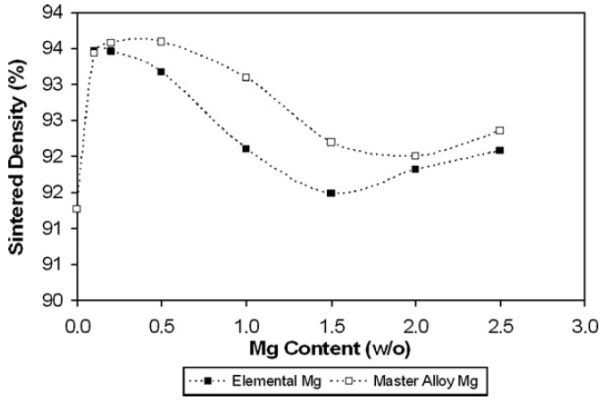

Figure 15: The effect of elemental and pre-alloyed addition of magnesium concentrations of 0.1%, 0.15%, 0.5%, 1.0%, 1.5%, 2%, and 2.5% on the sintered density of aluminum PM parts [60]

MacAskill *et al.* also observed the effect of tin (Sn) on the sintering behavior of aluminum in the absence and presence of the magnesium [60]. A noticeable decrease in the sintered density was observed when tin was added to the aluminum powders without the magnesium content. This suggests that the sole addition of tin is not an effective method to enhance the sintering behavior of aluminum. The significance of tin can be observed when it is added to the aluminum-magnesium mixture. Aluminum is completely soluble in a liquid tin whereas tin is sparingly soluble in solid aluminum. Since the surface tension of the liquid tin is significantly lower compared to the aluminum, a small amount of tin improves the wetting characteristic and sintering behavior of aluminum. This implies that tin is capable of reducing the surface tension of the liquid phase formed during the sintering process. As a result, the addition of tin in the aluminum-magnesium mixture significantly increased the sintered density of the part as shown in Figure 16.

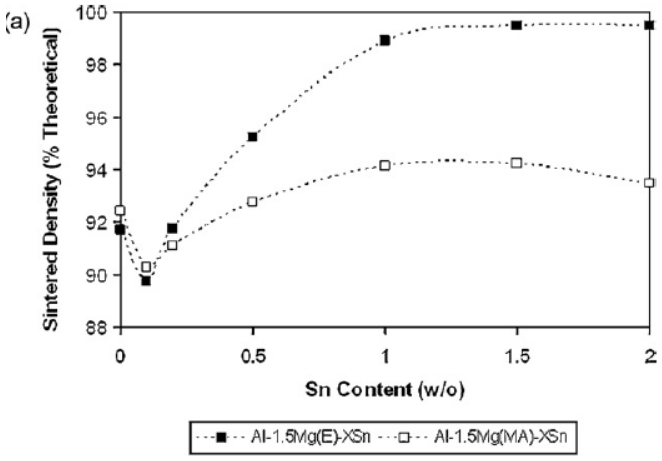

Figure 16: Sintered density of ternary Al-Mg-Sn mixture as a function of tin concentrations (0%, 0.1%, 0.15%, 0.5%, 1.0%, 1.5%, and 2%) [60]

Sintering behaviors of aluminum in argon and in nitrogen were observed by Liu *et al.* in 2008 [65]. The part sintered under argon atmosphere displayed clear dimensional distortions in contrast to the part sintered in nitrogen. High dimensional accuracy and enhanced structural rigidity of the nitrogen sintered part can be explained by the controlled grain size (See Figure 17). The grain size of the part sintered in argon ranges from 13 μm to 100 μm, where the original grain size of less than 20 μm was retained in nitrogen sintered sample. This is possible as the nitridation occurs along the grain boundaries to minimize the grain growth which limited the dimensional distortions.

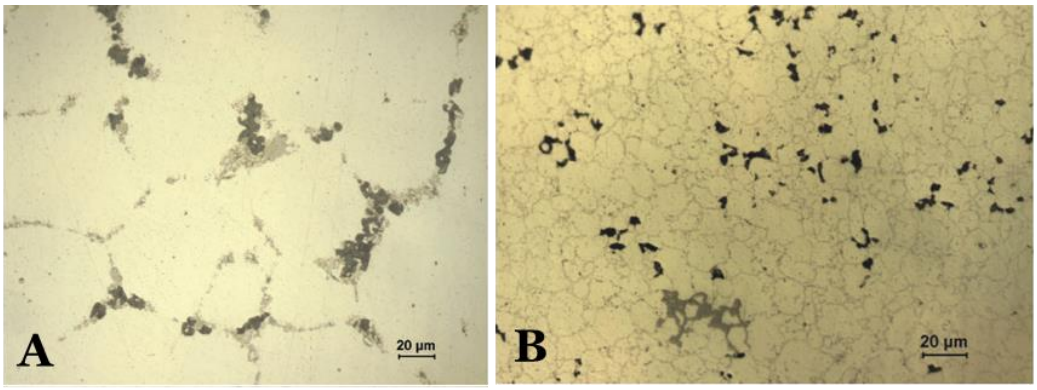

Figure 17: Optical micrographs of hot-pressed AA6061 with tin addition sintered at 620 ℃ for 1 hour, a) a part sintered in argon, b) the part sintered in nitrogen [65]

The addition of tin in the sintering mechanism for aluminum provides multiple advantages. As mentioned earlier in this section, it was observed that tin aids the wetting behaviors of the liquid-phase sintering. Moreover, it is also important to indicate that the rate and mechanism of nitridation can be controlled by adding tin in aluminum powders. In 2006, Sercombe and Schaffer identified the role of tin in the nitridation of aluminum powders [66]. The rapid growth of nitride both into and out from the surface of aluminum particles was observed without the tin content. In contrast, a small amount of tin significantly decreased the nitridation and controlled the formation sites. With the presence of tin, aluminum nitride formed along the grain boundaries and suppressed the grain growth.

2.4.2 *Metal Injection Molding of Aluminum alloys*

Metal injection molding (MIM) is a conventional technology used to shape metal powders into a complex geometry. The MIM is associated with four main processes including feedstock preparation, injection molding, de-binding, and sintering. The feedstock preparation is a step where the metal powders and liquified binders are mixed in a certain ratio. The mixed binders act as a medium for the molding process to improve the flow property of the feedstock. The feedstock is then injected into a mold to fabricate a part with the desired geometry. The molded part undergoes the de-binding process followed by a heat treatment cycle to sinter the part to high density [67].

The binders used for the MIM typically consist of lubricant, backbone binder, and a small quantity of surfactants. Each of these components in the binder system is closely linked to the critical properties of the binders. The lubricant improves the rheological properties of the powder-binder mixture. A low molecular weight polymer or wax is generally used for the lubricant to lower the viscosity of the binder. This assists in improving the wetting behavior of the binder and aids the mixing and molding process. The backbone binder is added to provide structural integrity of the green component until the onset of the sintering. To provide sufficient dimensional strength, thermoplastic polymers with high thermal stability

are generally employed. In addition to these major components, a small quantity of surfactants is often added to improve the interactions between the metal powders and binders. It also serves to enhance the flow property of the feedstock [68]. Although binders provide benefits during the fabrication process, it is required that binders be inert to the metal powders to avoid having any unwanted reactions. In addition, a complete burnout during the de-binding step without leaving any residues is another critical property that a successful binder system must have.

The typical lubricants used for the MIM of aluminum alloys are carnauba wax, palm oil wax, or paraffin wax. The high-density polyethylene (HDPE) and low-density polyethylene (LDPE) are common materials used as a backbone binder where the stearic acid is utilized as a surfactant [65],[67],[69],[70]. While there are studies available for processing aluminum alloys using the MIM technology, the applications using the BJ technology have not yet been extensively investigated even though the BJ is originated from the MIM process. There is a possibility of applying the binder system formulated for MIM on the BJ technology. However, based on the information available from the material safety data sheet (MSDS), it is evident that HDPE and LDPE which are popular in the MIM process are not suitable for the BJ due to their low solubility in the common solvents. It is important to note that polymers for the BJ process must have good solubility as the binders should be particle-free to avoid having a clog at the printhead nozzle. Hence, there is a need to further research on a polymer that is more suited to process aluminum alloys on the BJ technology.

The sintering process of the MIM generally involves the formation of a liquid phase to increase the final density of the part. For aluminum alloys, LPS is deemed more important as the formed liquid phase also assists with disrupting the oxide films of the aluminum particles. However, the use of LPS often leads to having larger part distortions due to the excess amount of liquid generated during the sintering process [71]. Unfortunately, this cannot be accepted in the BJ process since the thermal treatments are performed without any means of supports. Hence, the investigation of sintering agents that can disrupt the oxide films below the melting temperature of the aluminum powder is considered necessary.

3.0 Potential Binder and Sintering Agents for Aluminum Alloys

Recently, there has been a growing interest in processing aluminum alloys using the BJ technology. Since the BJ technology is still being actively researched, there are not many publications available about the binder system tailored for aluminum alloys. Therefore, this chapter is dedicated to suggests the options of binders and sintering agents for the binder jetted aluminum parts. The experimental studies using the introduced materials will be further explained in Section 4.0.

3.1 Binding Agents

A binding agent, also known as a binder, is a material that provides dimensional strength to shape powdered substances into the desired geometry. In the PIM industry, polymers are the most common binders that are widely used to bind many materials including pharmaceutical materials, ceramics, and metals [65], [67], [69], [70], [72], [73]. The polymers used in the PIM industry are well-known for providing good structural integrity to the molded parts with a long shelf life, competitive cost, clear burnout characteristics, and acceptable environmental hazard. Since the PIM and BJ share similar fundamental concepts, those advantages of the polymer binders are also applicable to the BJ process. Therefore, these binder types were accepted by the BJ industry without any major conflict [74].

Despite the importance of the binders in BJ technology, the current trend of the AM publications tends to emphasize the build parameters, powder rheology, or microstructure and mechanical properties of the printed part [19], [75]-[78]. Moreover, the research related to the binder compositions is often kept private due to the confidentiality. Therefore, to observe the compatibility of polymer binders and aluminum alloy, some of the popular polymers used in different fields of the industry are suggested for the current study. Polyvinylpyrrolidone and polyacrylic acid are recommended since they are highly compatible with the common organic solvents and are proven in industries for processing ceramics and pharmaceutical materials [72], [73], [79]-[81]. In addition, polyvinyl alcohol is suggested due to its high solubility in water, which could give a good opportunity in this research to explore the compatibility of aluminum powder with a water-based binder [82], [83]. The polymers that do not contain oxygen such as polyacrylonitrile and polyvinylidene fluoride are also selected to be studied in this research [84], [85]. These considered polymers have a different degradation temperature, which is expected to add a variety to this thesis to examine the effect of varying de-binding temperatures in the final quality of the sintered part.

Similar to the binders used for the MIM process, there are certain binder characteristics that must be satisfied to be considered as a successful binder system. In this thesis, only a few critical properties are considered. The binder must provide a sufficient green strength with a low de-binding temperature than the melting point of the aluminum powder. Moreover, the binder should be inert with the aluminum powders to avoid having any unwanted reactions. Hence, in this work, the success criteria of the binding agent will be limited to the degree of adhesion, complete removal, and densification of the final part.

The conventional polymer binders introduced in this chapter are highly compatible with many metal compounds. However, the use of these polymer binders causes several disadvantages which affect the quality of the final product. First, the sintering profile has to be extended to facilitate polymer pyrolysis

and degassing which increases the sintering duration. In addition, the structural integrity of the part can be affected if the polymer burnout temperature is in proximate to the sintering temperature of the metals. This is a critical challenge in sintering aluminum since the melting temperature of the aluminum is mostly very close to the de-binding temperature of the polymer binders. Moreover, unwanted residues of polymer binders can be trapped inside the parts and degrade the purity of the final product. To mitigate these disadvantages, the integration of the sintering agents such as nanoparticles or metallic salts gained the interest of the industry.

3.2 Sintering Agents

In Section 2.4, the hindrance of the oxide layer in sintering the aluminum powder and the conventional powder metallurgical approach in removing these layers were introduced. This chapter also suggested that magnesium and calcium as the only elements that can deoxidize aluminum oxide due to their higher affinity for the oxide (See Figure 13). However, this also makes the magnesium and calcium highly flammable in contact with air. This increases the risk of fire hazards and integrating these elements is not favorable to the manufacturing environment due to the increased safety concern. Therefore, this chapter is committed to providing an alternative approach for the oxide layer disruption. In the following chapters, two methods involving the use of nano-size particles will be introduced to study the possibility of the oxide layer interruption. The metallic and oxide nanoparticles dispersed in the polymeric binder and the metal-organic decomposition (MOD) ink are the candidates for this work. The MOD ink is anticipated to deposit nano-size particles upon the heat treatment. This work relies on the reactive nature of the nanoparticles in assisting with the disruption of the oxide films covering the aluminum powder.

3.2.1 *Metallic and Oxide Nanoparticle Dispersion*

The nanoparticles exhibit unique features compared to their bulk materials due to a high surface-to-volume ratio [86]. A significantly smaller particle size has a vast influence in changing various characteristics such as morphological properties, thermal properties, electromagnetic properties, optical properties, and mechanical properties [87]. The nanoparticles are also highly unstable and reactive since the high surface energy drifted it away from the equilibrium state. Hence, the nanoparticles often have a strong desire to be in a more stable state by reacting with other materials [88]. These interesting features fascinated many researchers and industries to develop the applications using the nanoparticles to benefit their processes. The BJ industry recently has entered this field of study to integrate the nanoparticles as a densifier to improve the final density and dimensional accuracy of the product.

One of the earliest studies of using the nanoparticles in the BJ process was published by Crane in 2005. To observe the effect of nanoparticles on the dimensional accuracy of the 410 stainless steel part, iron nanoparticle suspension was used as an infiltrate. The reported outcomes indicated a reduction in the part shrinkage by 60% [89]. Similarly, the effect on the mechanical property of the binder jetted alumina parts have been observed by Kunchala and Kappagantula in 2018. The alumina nanoparticles with an average particle size of 50 *nm* were suspended in the binder composed of the DI water and the PVA. The green density and the compression strength of the binder jetted parts with varying nanoparticle concentrations were the focus of the current study. An increasing trend in the green density and the compression strength was observed with the higher nanoparticle concentrations. Numerically, the overall increase of 30% in the green density, and 740% in the compression strength was reported by using the 15 *wt*% nanoparticle contents [90]. Recently, Bai and Williams also presented a study that utilized the copper nanoparticles for printing a copper component using the BJ technology. The study focused on observing the performance differences between the polymer binder and nanoparticle suspensions. In this study, three samples were prepared with (1) polymer binder as a control sample, (2) nanoparticle suspensions in the polymer binder to represent the colloidal sample and (3) nanoparticle suspensions in the non-adhesive medium for the analysis. In-bed curing was an added step of post-processing requirement for the parts that contained nanoparticles to provide green strength by promoting the sintering of the nanoparticles. The samples fabricated with nanoparticles demonstrated higher green density, lower carbon residuals, improved mechanical properties, and lower volumetric shrinkage. However, a higher nanoparticle loading was required to achieve a similar sintered density of the polymer binder.

As observed by the other researchers, integrating the nanoparticles in the BJ process presented a successful result by improving the density, mechanical performance, and dimensional accuracy of the printed part. In addition to the distinct benefits, the work published by Bai and Williams extended the possibility of replacing the conventional binding agent with the nanoparticles. Which will consequently shorten the sintering profile by eliminating the need for polymer pyrolysis and degassing. In this thesis, the primary objective is to introduce the nanoparticles to the aluminum alloys 1) to obtain advanced physical properties of the printed aluminum parts and 2) to investigate the potential ability to remove the oxide film on the aluminum particles. A highly reactive properties of nanoparticles manifested the possibility of disturbing the oxide layer on aluminum particles and forming the oxide to reach a more stable state.

3.2.2 *Metal-Organic Decomposition (MOD) Ink*

The formulation of metallic ink is comprised of metal salts and compatible solvents [92]. This type of ink was first developed to print conductive films for electronics. However, the researchers have seen the

potential of using these metallic inks to improve the sinterability of metals for the binder jetting process. The metallic ink is largely characterized into metallic salt nanoparticle dispersion and precursor-type. A simplified pictorial representation of the preparation process and printing mechanisms through the nozzle of both types of metallic ink is presented in Figure 18 [93]. In general, metallic salt nanoparticle dispersions provide higher metal loadings but there are critical disadvantages that prevent these dispersions to be considered as a competitive binder material. The two most critical disadvantages of employing metallic salt nanoparticle dispersions are (1) limitations on the printhead nozzle diameter based on the size of the nanoparticles that confines the minimal feature size and (2) the tendency to clog the printhead nozzle which requires frequent maintenance and degrade the quality of the product [93]. By contrast, MOD ink is a particle-free solution that can bypass these disadvantages. The thermal decomposition of MOD ink occurs at an elevated temperature and deposits solid metals on the powder bed upon heating. Therefore, MOD ink can be a sustainable material that has the potential to reduce the challenges of metallic salt nanoparticle dispersions. MOD ink is formulated by dissolving the metal precursor in the solvents and organic complexing agents (ligands) to form an organometallic compound. Depending on the properties of the metal precursor, solvents such as xylene or mixed alcohols are used to formulate the MOD ink. In addition, complexing agents such as amino hydroxyl compounds or carboxylic acids are also added to serve a few purposes [93]. The complexing agents help to improve the solubility of the metal-organic compounds in solvents and lowers the decomposition temperature of the metallic ink [92].

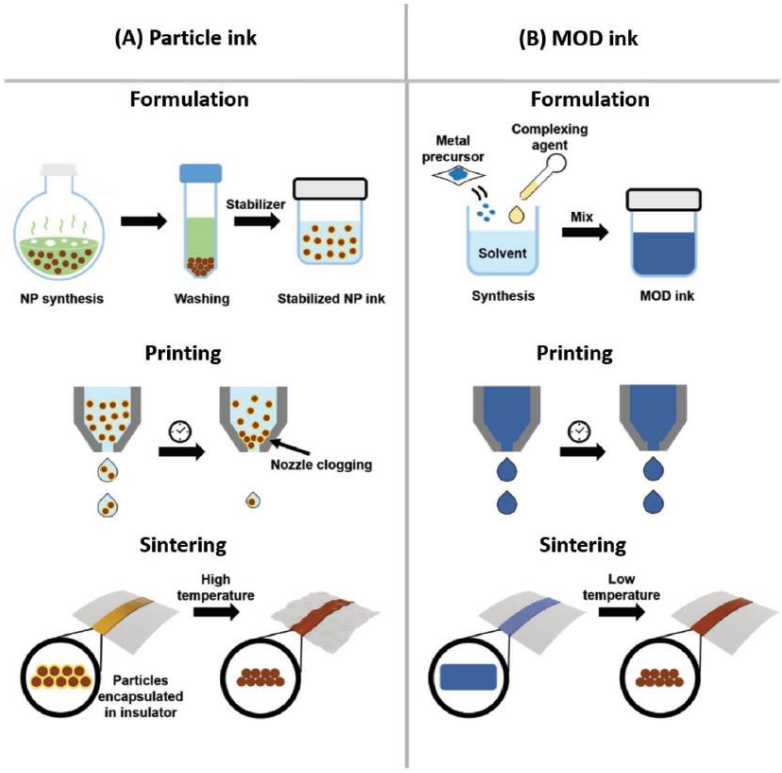

Figure 18: Formulation process and printing mechanism of a) nanoparticle ink, b) MOD ink illustrated by Choi et al. [93]

In 2018, Bai and Williams investigated the compatibility of the MOD ink on the binder jetting process by studying the changes in sintered density and porosity of the copper part [92]. In this analysis, copper formate was used as a metal precursor to precipitate the solid metals between the micron-sized copper particles during the sintering process. Compared to the samples printed with the conventional polymer binders, a decrease in the sintered density was observed. It was noted that the green state of the MOD ink printed part suffered from a lower green state strength. As a result, the edge of the parts was damaged during the de-powdering process and lowered the final density. However, a significant decrease in the concentration of porosities was observed when only the core sections of the printed part were compared (see Figure 19). This result was obtained as the deposited nanoparticle metals promoted the densifying effects on the powder bed. Therefore, it indicates that MOD ink can be used as an alternative to polymer binder to improve the dimensional stability and density of the binder jetted parts with a modification to improve the green state strength [92].

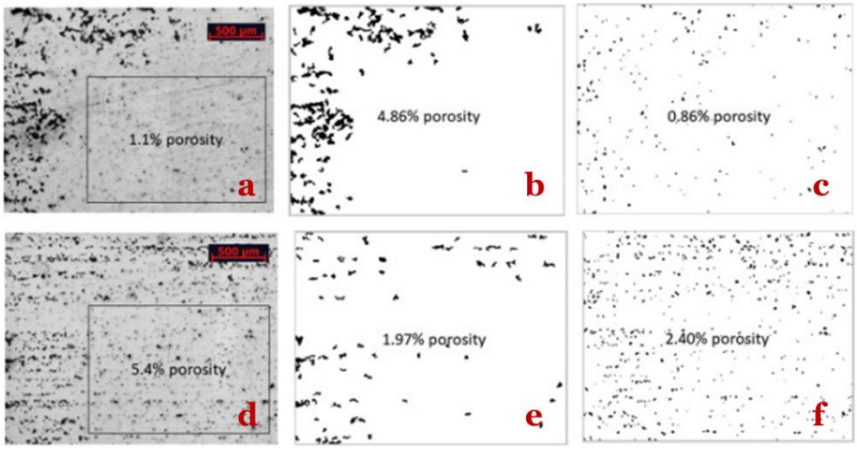

Figure 19: The porosity measurement of MOD ink and polymer binder printed parts where (a)-(c) MOD printed parts and (d)-(f) polymer printed parts, (a, d) core sections only (1.1%), (b, e) large pores, and (c, f) small pores prepared by Bai and Williams [92]

As observed by Bai and Williams, MOD ink poses a great potential to enhance the dimensional accuracy and density of the printed part. Therefore, in this research, the role of copper and silver MOD ink in disrupting the oxide layer will be investigated. Although it is known that copper and silver are less reactive than aluminum in bulk quantity, the thermodynamics of these nanoparticles remains unknown. An interesting physical and chemical properties of nanomaterials have been previously observed from multiple literatures [94], [95]. In these literatures, it has been revealed that nanoparticles are extremely unstable due to the vast surface-to-volume ratio [96]. Hence, it is possible that nanoparticles may experience a higher affinity to form the oxide to reach a relatively stable state. The low decomposition temperature and competitive cost are another consideration that will be used to evaluate the MOD inks.

Silver is the most common metal precursor for the MOD ink due to its low resistivity ($1.59\ \mu\Omega \cdot cm$) and high stability from oxidation [92]. The ease of handling and the high-quality conductive films are other attractions of using the silver MOD ink. A summary of publications on the silver MOD ink by using various silver precursors is shown in Table 2.

Table 2: A summary of researches on Silver MOD inks

Precursor	Complexing agents, additives, and solvents	Decomposition temperature	Ref.
Silver acetate	Ethylamine, ethanolamine, 2-hydroxyethyl-cellulose, water, formic acid	150 ℃	[97]
Silver citrate	1,2-diaminopropane, isopropanol	150 ℃	[98]
Silver hexa-fluoroacetylacetonate	Isopropanol toluene	120 ℃	[99]
Silver neodecanoate	Xylene	150-200 ℃	[100]
Silver oxalate	Ethylamine, ethylene glycol, EtOH	150 ℃	[100]

While the silver MOD ink remains as the most preferred material, there has been an increasing demand from industry to develop cost-efficient MOD inks for a greater profit. Copper was suggested as the best candidate due to its low resistivity ($1.72\ \mu\Omega \cdot \mathrm{cm}$) next to the silver and significantly lower cost [92]. Copper MOD ink is often stored in the oxidized form to prevent rapid oxidization in the air for more accessible handling. The list of literatures on the copper MOD ink is summarized in Table 3.

Table 3: A summary of researches on Copper MOD inks

Precursor	Complexing agents, additives, and solvents	Decomposition temperature	Ref.
Copper acetate	Isopropanolamine, IPA, ethanol	150 ℃	[102]
Copper formate	AMP, methanol	350 ℃	[103]
Copper formate tetrahydrate	IPA	120 ℃	[102]
Copper (II) formate tetrahydrate	Hexylamine	200 ℃	[104]
Copper hydroxide	Diethylene glycol 2-amino-2-methyl propanol formic acid, ethanol	200 ℃	[105]

Aforementioned at the beginning of this section, the focus of this thesis is to identify the most compatible binding agent and sintering agent for the aluminum alloys. The first part of the study involves experimenting different binding agents to discover its ability to provide dimensional strength to the aluminum parts without leaving a subsequent amount of residuals. The second part consists of integrating sintering agents as a 1) promising alternative to the binding agent and 2) potential sintering mechanisms for the aluminum alloys.

4.0 Experimental Methods

4.1 Materials

AlSi10Mg powder (SLM Solutions, Germany, ρ: 2.67 g/cm^3) with a mean particle size of 42 μm was used as a base material. The chemical composition of the AlSi10Mg powders is shown in Table 4.

Table 4: The composition of AlSi10Mg in a mass fraction [%]

Al	Si	Fe	Cu	Mn	Mg	Zn	Ti	Ni	Pb	Sn	Other
Bal.	9.00-11.00	0.55	0.05	0.45	0.20-0.45	0.10	0.15	0.05	0.05	0.05	0.15

Polyvinylpyrrolidone (PVP), poly(vinyl) alcohol (PVA), polyacrylic acid (PAA), polyacrylonitrile (PAN), and polyvinylidene fluoride (PVDF) with an average mol. wt. of 40,000, 31,000 to 50, 000, 450,000, 150,000, and 534,000 were purchased from Sigma Aldrich (MO, USA). These polymers were acquired to formulate the binding agent with dimethylformamide (DMF), 2-propanol, and DI water. DMF (M_w: 73.09 g/mol, 99.8% purity) and 2-propanol (M_w: 60.10 g/mol, 99.5% purity) were also purchased from Sigma Aldrich.

The copper oxide (CuO, 80 nm, 99% purity), aluminum oxide (Al_2O_3, 80 nm, 99.5% purity), and copper (Cu, 40 nm, 99.9% purity) NPs were obtained from US Research Nanomaterials, Inc (TX, USA) to prepare NPs suspensions. The MOD ink formulation procedures were obtained from the literatures. The method developed by Nie *et al.* was accepted in this thesis to prepare the silver (Ag) MOD ink [98]. The required chemicals for this experiment were 1,2-diaminopropane (M_w: 74.13 g/mol, 99% purity) and silver (I) citrate hydrate (M_w: 512.70 g/mol, 98% purity) which were purchased from Alfa Aesar (MA, USA). The copper (Cu) MOD ink preparation method was obtained from the study published by Shin *et al.* [103]. The chemicals involved in this method include the copper (II) formate tetrahydrate (M_w: 225.65 g/mol, 98% purity) purchased from Alfa Aesar, and 2-amino-2-methyl-1-propanol (AMP) (M_w: 89.14 g/mol, ≥95% purity) and methanol (M_w: 32.04 g/mol, ≥99.6% purity) from Sigma Aldrich.

4.2 Sample Fabrication

4.2.1 *Sample Preparation*

The liquid binders were prepared by mixing the polymer and solvent in a certain ratio. In this work, five solutions were formulated with a different compositions: PVP:2-propanol (5:95), PVA:DI water (2:98), PAA:2-propanol (0.5:99.5), PAN:DMF (5:95), and PVDF:DMF (3.5:96.5). These prepared solutions were mixed using the magnetic stirrer, H3760-HS, (Benchmark Scientific, NJ, USA) for 60 minutes to completely dissolve the polymer powders. The NP dispersions were obtained by dispersing 0.5, 1, 2, and 5% of each NPs in the selected binder based on the binder characterization result. The dispersions were sonicated on VWR 250-T ultrasonic cleanser (VWR International, PA, USA) for 30 minutes to break the particle agglomerates.

The Ag and Cu MOD ink formulation procedures were obtained from the literatures presented by Nie *et al.* and *Shin et al.*, respectively. A synthesized silver (I) citrate hydrate was purchased to make the Ag MOD ink. As observed in Figure 20, a mixture that contains methanol (5 ml), isopropanol (3 ml), and 1,2-

diaminopropane (2 ml) were prepared and incubated at 10 ℃ for 15 minutes. After the solvents were prepared, 2g of silver (I) citrate hydrate was dissolved in the mixed solvent and stirred for 1 hour at 10 ℃. The obtained ink was diluted in 2-propanol to acquire 2 and 5% of silver particles in the sample upon the heat treatment.

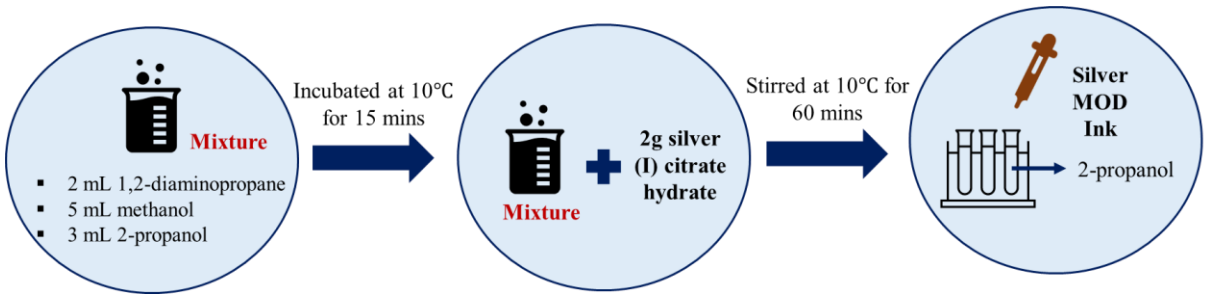

Figure 20: A schematic of the Ag MOD ink formulation procedures

A process map for fabricating the samples with the Cu MOD ink is summarized in Figure 21. The mix of solvents consisting of methanol (30 mL) and AMP (25 mL) was stirred for 30 minutes on the magnetic stirrer. The copper (II) formate tetrahydrate (29.3 g) was added to the mixture and stirred for 1 hour until the solution was homogenized. To extract the excess methanol and water, the solution was heated on the heating plate, H3760-HS (Benchmark Scientific, NJ, USA) for 15 hours at 60 ℃. After the extraction, an obtained paste was diluted in 2-propanol to build test specimens with deposited 0.1, 0.5, 1, and 5% of copper particles after the heat-treatment.

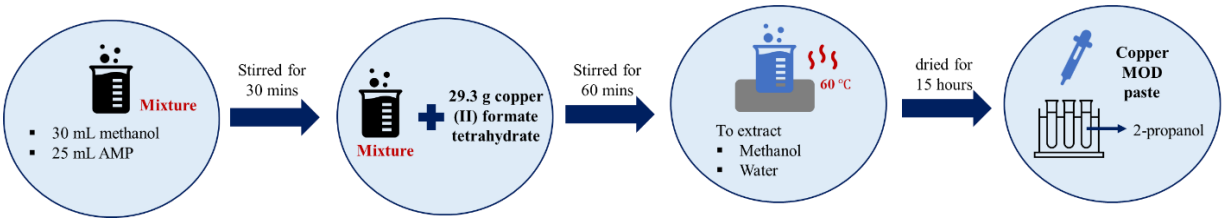

Figure 21: A schematic of the Cu MOD ink formulation procedures

The test specimens were manually fabricated by imitating the BJ process using the prepared solutions. A thin layer of the base materials was added layer by layer, and liquid binders or sintering agents were applied to each layer until the desired geometry was attained. For each layer, 30 to 45 seconds of the vibration was applied using the vibrating table (5817K15, McMaster-Carr, IL, USA) to evenly spread the liquid on the powder bed. The fabricated test specimens were cured on the heating plate at 60 ℃ for 12 hours and an example of the green specimens are shown in Figure 22.

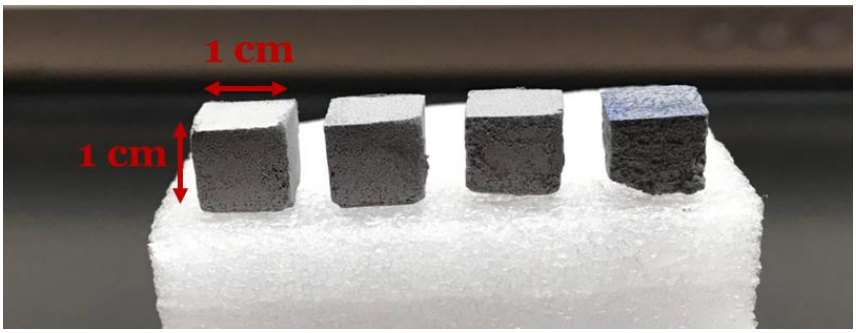

Figure 22: 1 cm cubes of the green specimens fabricated with copper mod inks

4.2.2 *Heat Treatment*

The sintering cycles were performed using the hybrid muffle furnace (KSL-1200X-H-UL) from the MTI Corporation (CA, USA) which the schematic of the furnace is shown in Figure 23a. The quartz tubes located at the back of the furnace were utilized for this study to create a contained environment (See Figure 23b). The de-binding phase was carried out in a vacuum with a low vacuum pressure ($\leq 10\ torrs$) to ensure a complete pyrolysis of the binding agents. After the de-binding phase, the atmosphere was changed to the flowing nitrogen gas (N2, 99.9% purity, Praxair, CT, USA) with a flow rate of 40 mL/min.

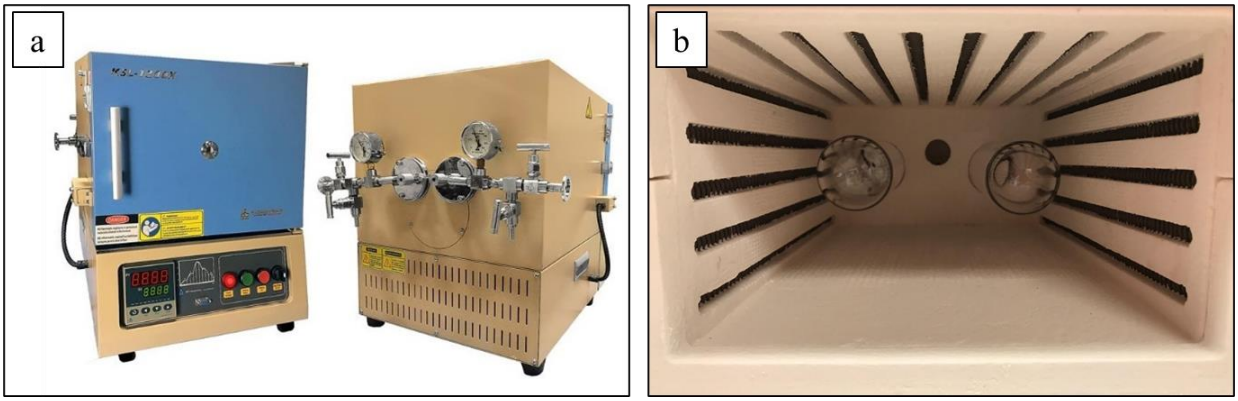

Figure 23: a) Schematic of the muffle furnace, KSL-1200X-H-UL, and b) the interior of the muffle furnace with quartz tubes installed

An illustration of the sintering profile is shown in Figure 24. The heating rate (5 ℃/min), de-binding or curing durations (60 $mins$), and sintering duration (240 $mins$) were kept constant for all test specimens to eliminate the influence of other factors in analyzing the effects of different binding and sintering agents. As stated in the literature, the curing temperatures of 150 and 175 ℃ were used for Ag and Cu MOD inks, respectively. The de-binding temperatures and sintering temperature were identified through the thermal analysis, and it will be further discussed in Section 5.1.

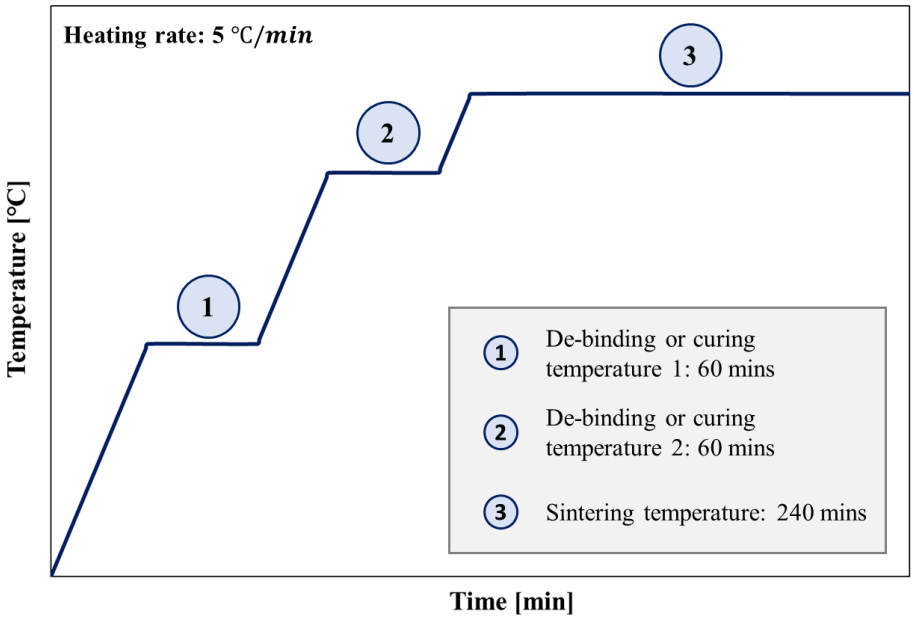

Figure 24: Typical sintering profile used in this study to sinter the test specimens

4.3 Material Characterization

4.3.1 *Thermal Properties of the Materials*

The thermal properties of the polymers and AlSi10Mg were analyzed to identify the sintering profile for the test specimens using the thermogravimetric analysis (TGA) and differential scanning calorimetry (DSC). TGA is a method that is used to obtain the thermal properties of the sample by measuring the mass over an increasing temperature. In this experiment, TA Instrument Q500 (New Castle, DE, USA) was used to analyze the degradation temperature of the binding agents (PVP, PVA, PAA, PAN, and PVDF). Air was used as a test atmosphere with a flow rate of 60 *mL/min,* and specimens were heated at 10 ℃/*min*.

DSC is a technique used to analyze the thermal properties of the sample by measuring the temperature and heat flow associated with the phase transitions. As the temperature changes, DSC calculates the differences in the thermal energy between the sample and the reference material as a function of time and temperature to obtain the heat flow. This test was completed on the Labsys Evo (Setaram, NJ, USA) using the DTA rod to determine the melting temperature of the AlSi10Mg with flowing argon gas at 15 *mL/min.*

4.3.2 *Elemental Analysis*

The elemental analyses were performed to evaluate the elemental compositions in the test specimens fabricated with the binding agents after the de-binding. A raw AlSi10Mg powder heat-treated at 500 ℃

was also analyzed as reference material. This test was conducted using the ONH 836 and CS 844 (LECO Corporation, MI, USA) to quantify the carbon and oxygen compositions. The utilized ONH 836 equipped with infrared and thermal conductivity detectors is designed to measure the oxygen, nitrogen, and hydrogen content from the material by applying the inert gas fusion technique [106]. In contrast, CS 844 detects carbon and sulfur by using combustion infrared detection [107]. The experiment was conducted by using helium and oxygen gas as carrier gas on ONH 836 and CS 844, respectively.

4.3.3 *Microscopic Characterization*

To determine the density of the sintered specimen, optical micrographs were taken using the Keyence VHX-7000 white light optical microscope (Osaka, Japan). The sintered test specimens were mounted, ground, and polished for observation. ImageJ, an image analysis program was utilized to calculate a total area of porosity on the cross-sectional surfaces of the specimens. A schematic of the analysis steps is shown in Figure 25.

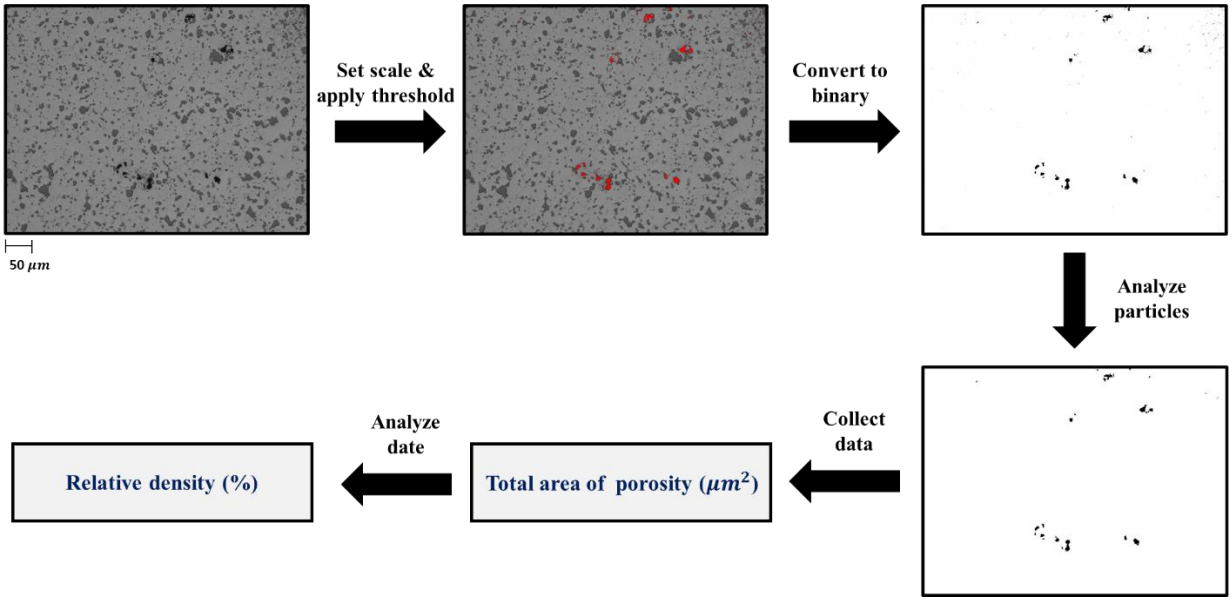

Figure 25: Image analysis map using ImageJ to obtain the sintered density of the test specimens

The micrographs at a higher magnification were obtained by performing the JEOL JSM-7600F field emission gun scanning electron microscope (FEG-SEM) equipped with Oxford Instruments X-Max 80 mm energy-dispersive X-ray spectroscopy (EDX) to observe the effect of sintering agent on sintered microstructure. Important sintering aspects such as neck formation or pore elimination were identified to help understand the efficiency of the sintering agents. In addition, the chemical compositions were analyzed by conducting the EDX at different locations in the micro-level to determine the composition of the prior particle boundaries and mechanisms associated with sintering.

5.0 Results and Discussions

5.1 Determination of the De-binding and Sintering Temperatures

TGA curves shown in Figure 26 were used to identify the polymer degradation temperatures to develop the de-binding schedules. The observations were extrapolated according to the standard ISO 11358-1. A tangential line on the starting mass and the maximum gradient on the TGA curve were intersected to find the point of intersection. The determined values are summarized in Table 5.

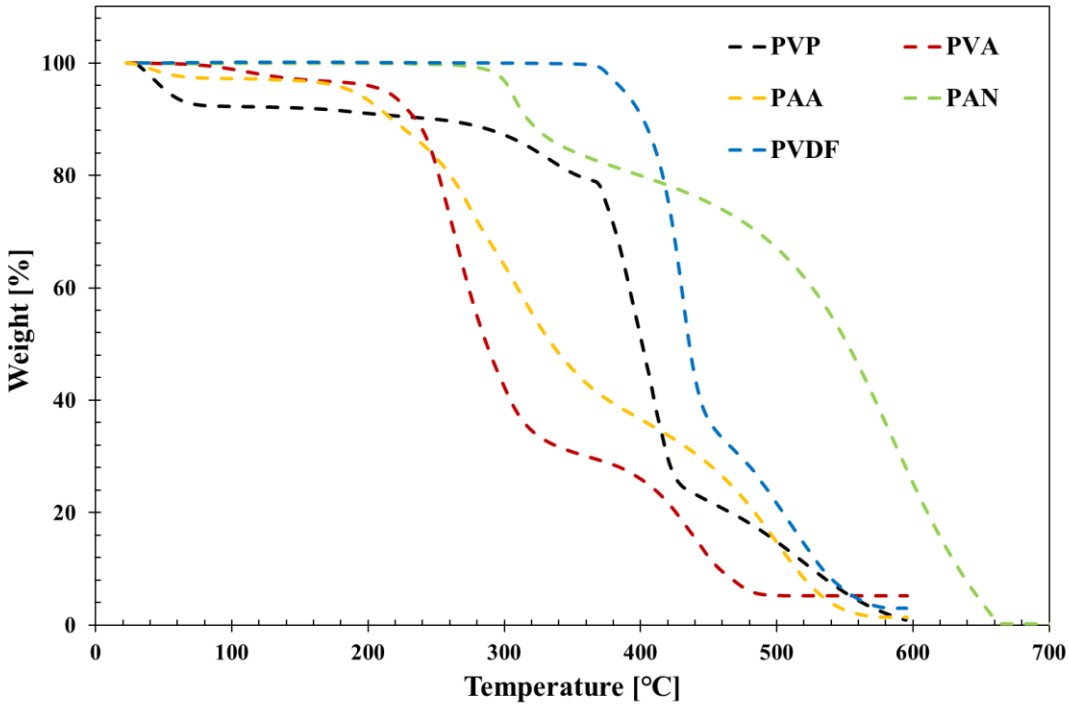

Figure 26: TGA curves of binding agents: PVP, PVA, PAA, PAN, and PVDF

Table 5: De-binding temperatures of the binding agents: PVP, PVA, PAA, PAN, and PVDF

Polymers	De-binding temperature 1 [℃]	De-binding temperature 2 [℃]
PVP	375	485
PVA	245	405
PAA	265	460
PAN	295	500
PVDF	410	480

To identify the melting properties of AlSi10Mg powders, DSC curves were interpreted based on the standard ISO 11357-1. The measured solidus and liquidus temperatures were 574 and 609 ℃,

respectively. The experimental values agreed with the literature values presented in Table 6. Based on this analysis, 550 ℃ was selected to be used as a sintering temperature.

Table 6: Solidus and liquidus of AlSi10Mg

AlSi10Mg	Solidus [℃]	Liquidus [℃]
Literature	577	616
Experimental	574	609

5.2 Investigation of the Residue Carbon and Oxygen Contents After the De-binding cycle

The specimens fabricated with the binding agents were evaluated to observe the residue carbon and oxygen contents after the thermal de-binding cycles. Each binding agents were de-bounded using different de-binding schedules as outlined in Table 5. The obtained values from the elemental analyzers are summarized in Table 7. A heat-treated AlSi10Mg powder at 500 ℃ was used as reference material to isolate the actual residual values. The determined carbon and oxygen contents of the AlSi10Mg were 0.024% and 0.114%, respectively, and these values were removed from the data in Table 7.

Table 7: Residual carbon and oxygen contents evaluated on the elemental analyzers

Polymers	Carbon content [%]	Oxygen content [%]
PVP	0.008	0.001
PVA	0.096	1.886
PAA	0.000	0.000
PAN	0.146	0.066
PVDF	0.061	0.006

The lowest residual contents were observed with the PAA specimens, where the highest oxygen contents were found with the PVA and the highest carbon contents in the PAN specimens. It was evident that the binding agents, except for the PAA, leave a residual on the sample even after the de-binding cycles. This may be a consequence of wrong de-binding temperatures, insufficient hold duration, or property of the binder. However, a more extensive study may be required to conclude the reasons behind the residual depositions inside the samples.

5.3 Porosity Analysis of Sintered Specimens

5.3.1 *Binding Agents*

The optical micrographs were obtained to observe the porosity network and the density of the test specimens. Figure 26 shows the micrographs of the samples fabricated with the binding agents, and the corresponding densities are summarized in Table 8. PVDF specimens were excluded in this study due to its inability to provide sufficient green strength. The interconnected pores with a lack of neck formation were observed in specimens with relatively lower sintered densities (PVA and PAA). In contrast, clear evidence of pore isolation and elimination were noticed with the specimens that achieved higher sintered densities (PVP and PAN). However, the PVP was the only binding agent that provided sufficient adhesions to promote the sintering to achieve a density higher than 95%.

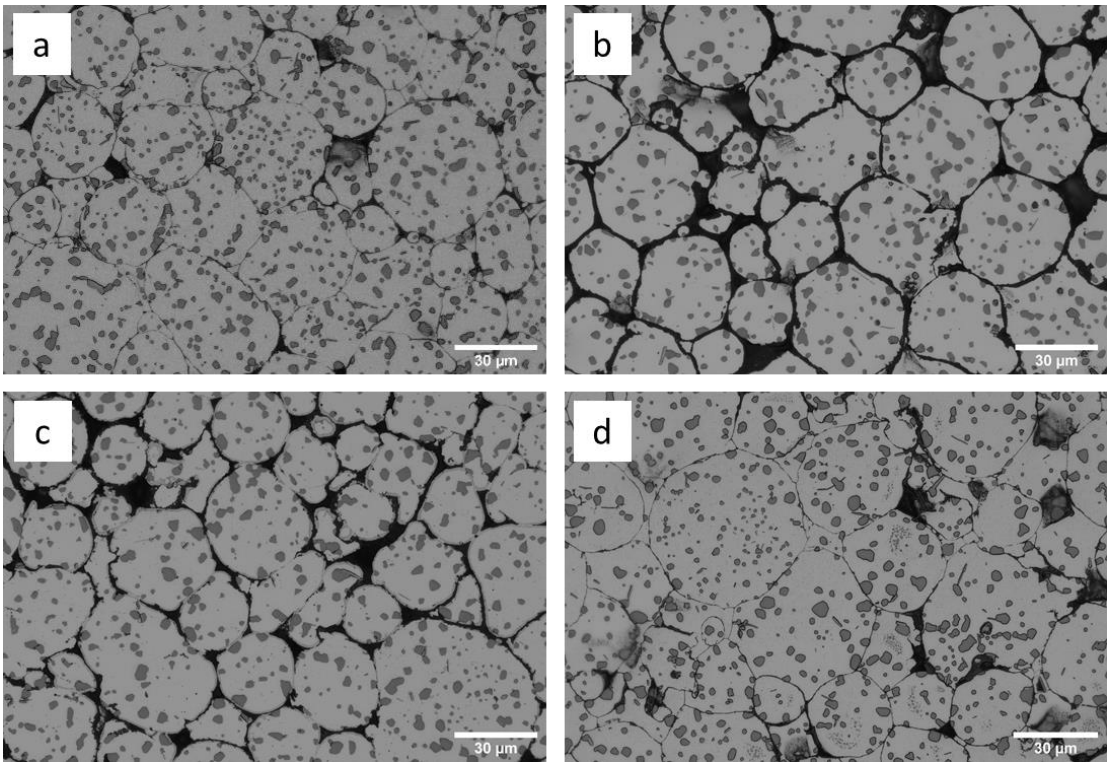

Figure 27: Optical micrographs of a) PVP, b) PVA, c) PAA, and d) PAN specimens sintered at 550 ℃ for 240 minutes

Table 8: Green and sintered relative densities of the specimens fabricated with PVP, PVA, PAA, and PAN

Polymers	Green density [%]	Sintered density [%]
PVP	63.5	95.1
PVA	63.1	87.5
PAA	61.3	87.7
PAN	63.9	90.6

5.3.2 *Metallic and Oxide Nanoparticles Dispersions*

Initially, nanoparticle dispersions were prepared to construct samples without the binding agents. However, this attempt presented an unsuccessful result in binding AlSi10Mg powders. Hence, to provide minimal structural integrity to process nanoparticle samples through the sample fabrication chain without leaving any unwanted residuals, the PAA binder with 0.5 *wt*% in 2-propanol was used as a base solution.

The overall comparison of the sintered densities of the AlSi10Mg specimens fabricated with nanoparticle dispersions is shown in Figure 28. In general, an incremental trend of the sintered density was observed as the nanoparticle concentration increased. It was also noticed that the specimen with the aluminum oxide showed a superior performance among the considered materials in the current study. The optical micrographs and densities of specimens fabricated with copper oxide, aluminum oxide, and copper nanoparticle dispersions are displayed in Figure 29 - Figure 31 and Table 9 - Table 11, respectively. The indication of pore isolation and elimination were visible in all test conditions.

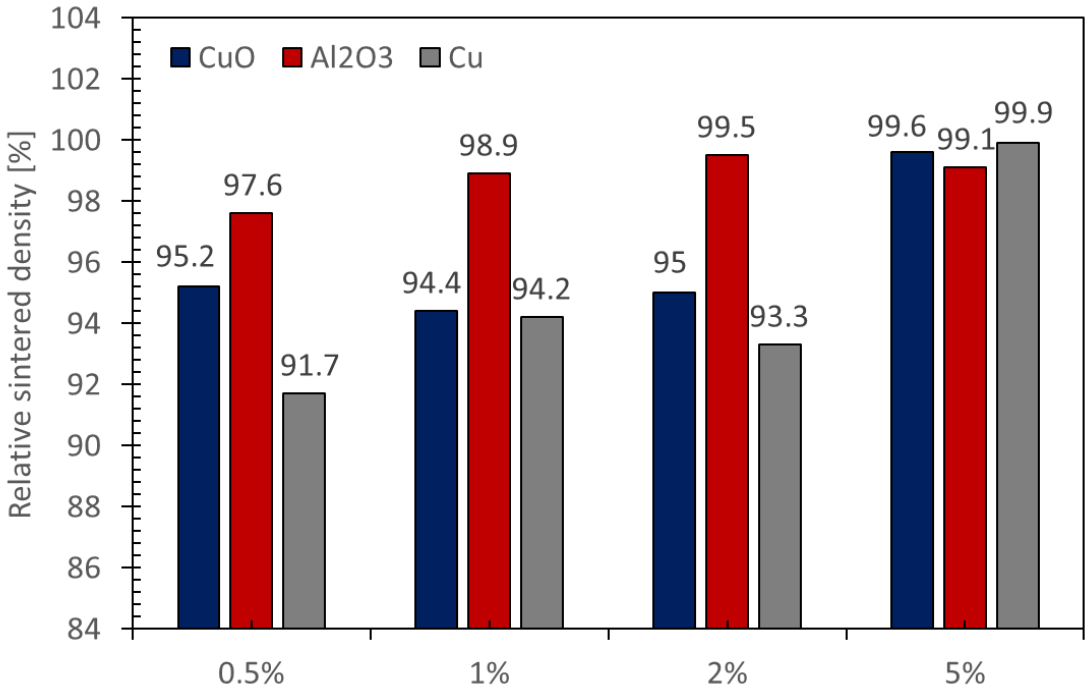

Figure 28: A summary of sintered densities of test specimens fabricated with copper oxide, aluminum oxide, and copper nanoparticle dispersions with varying concentrations

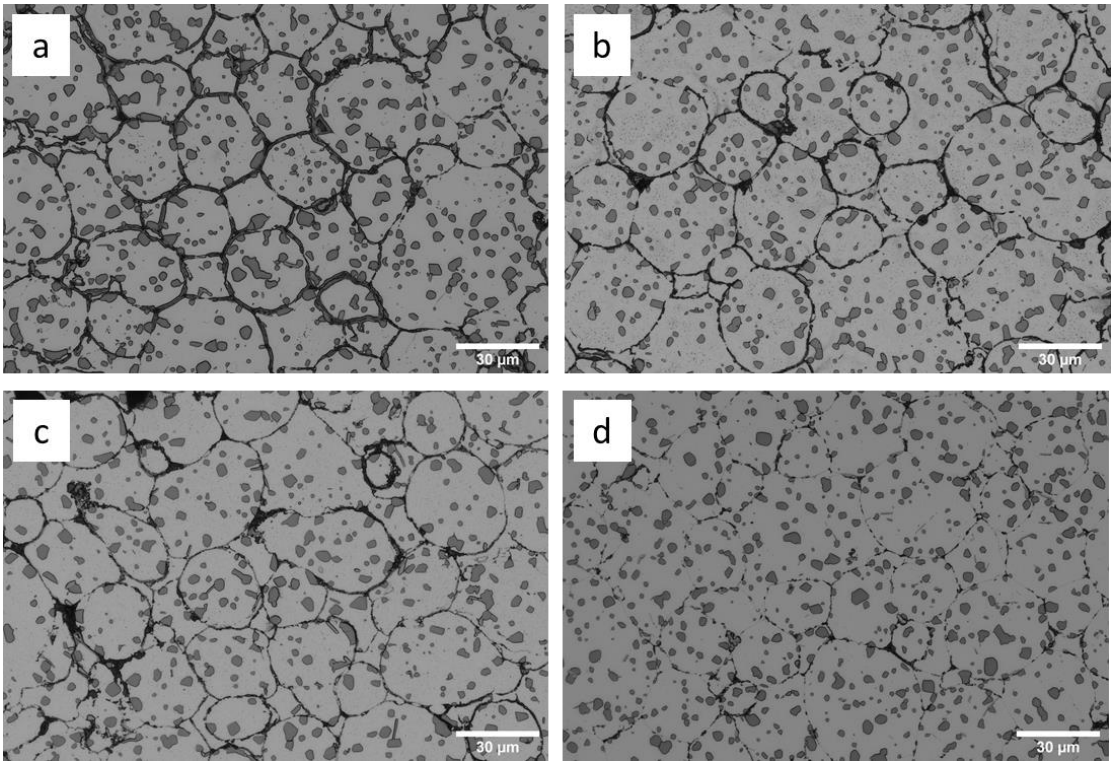

Figure 29: Optical micrographs of AlSi10Mg specimens fabricated with a) 0.5, b) 1, c) 2, and d) 5% copper oxide nanoparticle dispersion

Table 9: Green and sintered relative densities of AlSi10Mg specimens fabricated with a) 0.5, b) 1, c) 2, and d) 5% of copper nanoparticle dispersion

Sample ID	Green density [%]	Sintered density [%]
a	60.4	95.2
b	60.2	94.4
c	59.3	95.0
d	58.9	99.6

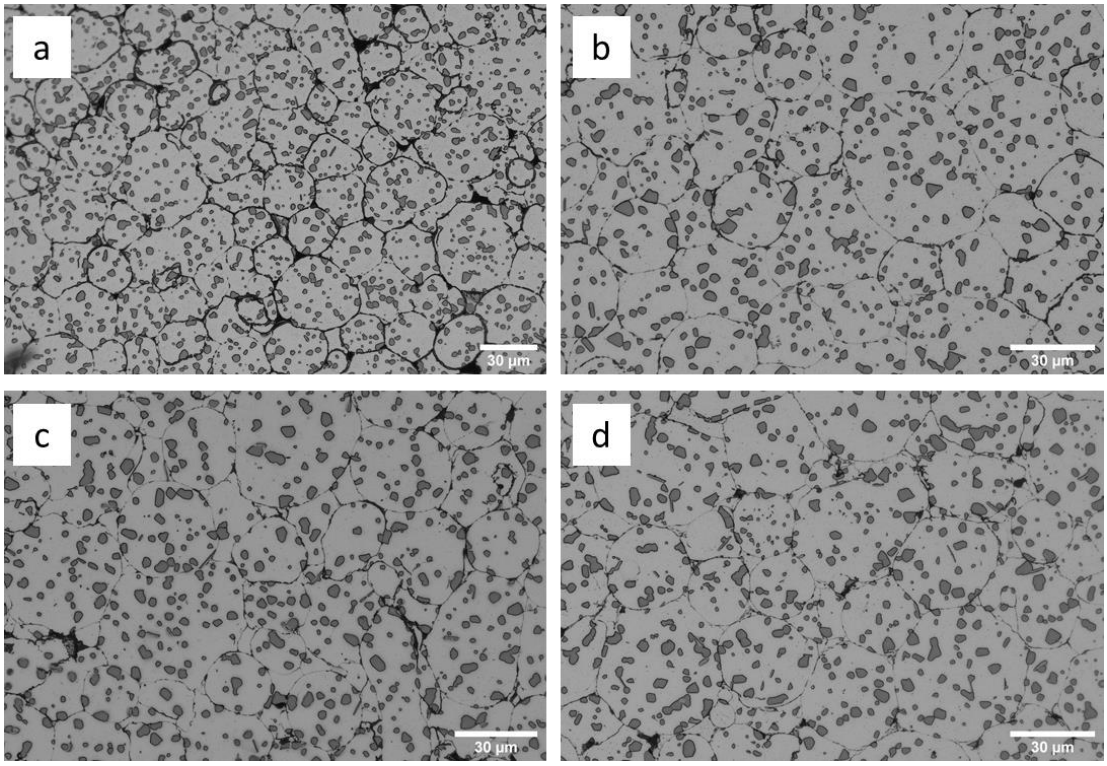

Figure 30: Optical micrographs of AlSi10Mg specimens fabricated with a) 0.5, b) 1, c) 2, and d) 5% aluminum oxide dispersion

Table 10: Green and sintered relative densities of AlSi10Mg specimens fabricated with a) 0.5, b) 1, c) 2, and d) 5% of aluminum oxide dispersion

Sample ID	Green density [%]	Sintered density [%]
a	60.3	97.6
b	60.3	98.9
c	60.9	99.5
d	58.4	99.1

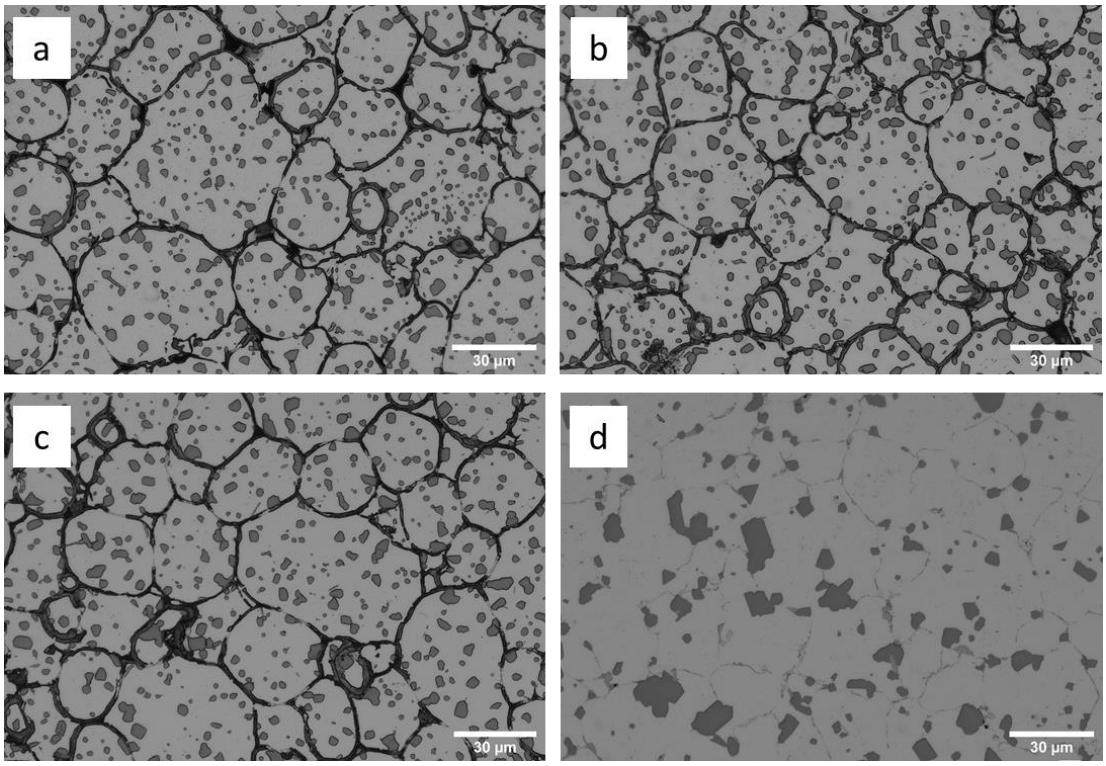

Figure 31: Optical micrographs of AlSi10Mg specimens with a) 0.5, b) 1, c) 2, and d) 5% copper nanoparticle dispersion

Table 11: Green and sintered relative densities of AlSi10Mg specimens fabricated with a) 0.5, b) 1, c) 2, and d) 5% copper nanoparticle dispersion

Sample ID	Green density [%]	Sintered density [%]
a	56.3	91.7
b	62.4	94.2
c	62.5	93.3
d	55.4	99.9

In Section 3.2.1, it was suggested that the nanoparticles may have an influence on disrupting the oxide layer due to its unstable nature. Since the oxide layer is known to prevent the sintering process, the full densification can be accepted as an indication that the oxide layer was successfully disturbed. However, to better understand the role of the nanoparticles, the SEM and the EDX will be followed in Section 5.4.

5.3.3 *Metal-Organic Decomposition (MOD) Inks*

The Ag MOD ink specimens demonstrated poor physical properties as shown in Figure 32. Large sections of the samples were dominated by network of porosities which reflects an inability of the Ag MOD ink in promoting the sintering. A coherent result was displayed through the porosity analysis, where only a 15.6% increase in the density was observed (See Table 12). The green density of the Ag MOD - 2% is not

available due to poor structural integrity in the green state. This indicates that the Ag MOD ink is an ineffective method to process the AlSi10Mg powders. Therefore, this test conditions will not be considered further study in this thesis.

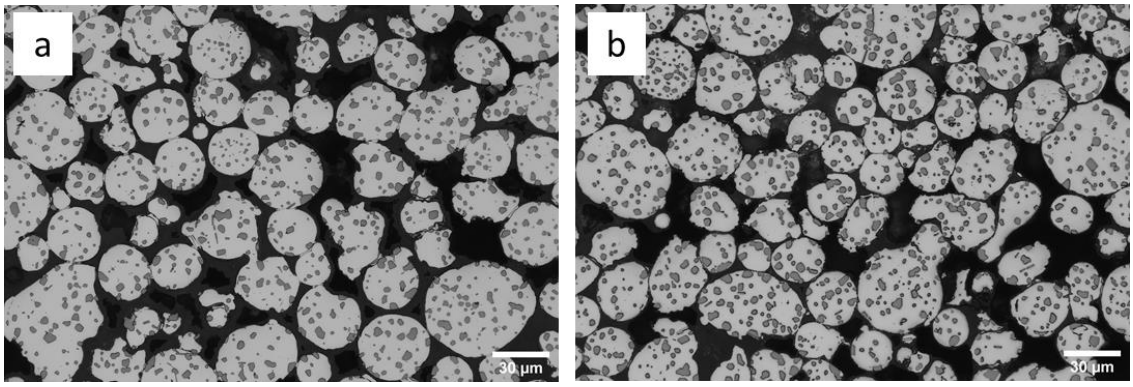

Figure 32: Optical micrographs of AlSi10Mg specimens with a) 2 and b) 5% silver MOD ink

Table 12: Green and sintered relative densities of AlSi10Mg specimens fabricated with a) 2 and b)5% silver MOD ink

Sample ID	Green density [%]	Sintered density [%]
a	–	70.5
b	56.7	72.3

The integration of Cu MOD ink displayed promising results as illustrated in Figure 33 and Table 13. A significant improvement in sintered density and microstructure was observed with a clear indication of pore elimination except for Figure 28a where only 0.1% of Cu MOD ink was used. The grain size growth was also noticed with the higher concentration of Cu MOD ink. The obtained micrographs and densities indicate that deposited Cu particles played an important role in disrupting the oxide layer. To understand this relationship, the SEM and the EDX analyses were performed and will be discussed in Section 5.4 alongside with the nanoparticle dispersions.

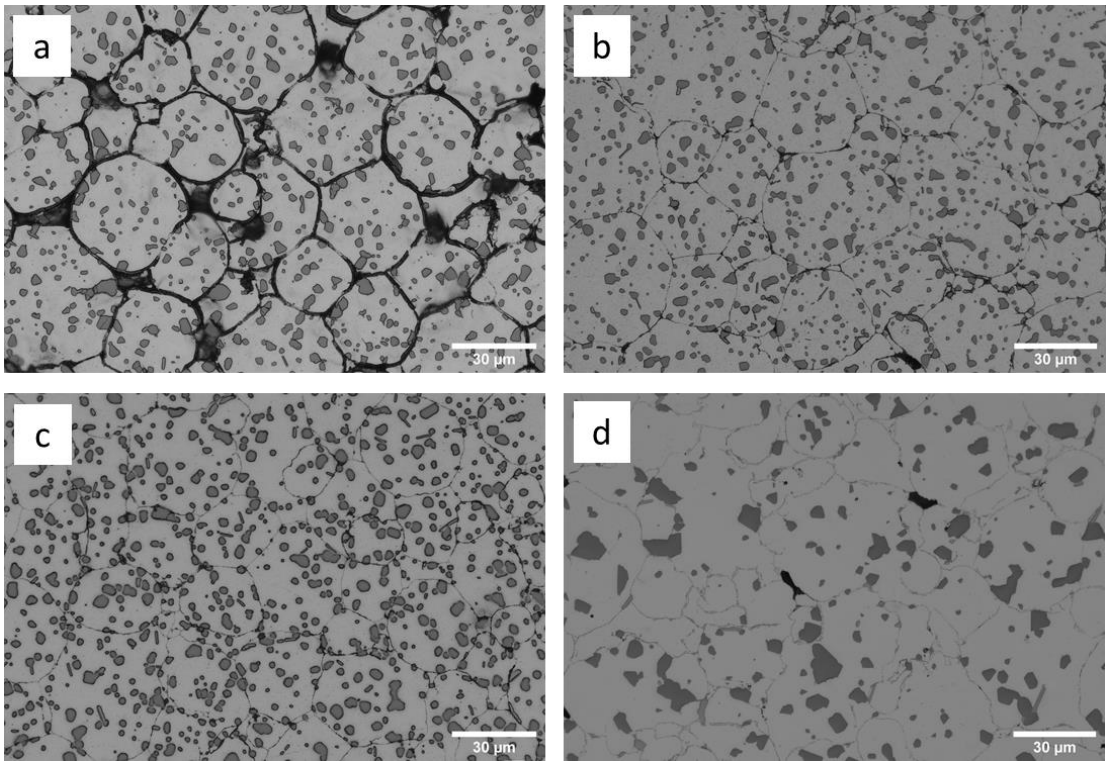

Figure 33:Optical micrographs of AlSi10Mg specimens with a) 0.1, b) 0.5, c) 1, and d) 5% Cu MOD ink

Table 13:Green and sintered relative densities of AlSi10Mg specimens fabricated with a) 0.1, b) 0.5, c) 1, d) 5% Cu MOD ink

Sample ID	Green density [%]	Sintered density [%]
a	61.8	90.8
b	64.8	99.6
c	65.4	99.9
d	65.9	99.7

5.4 Microstructure Analysis

5.4.1 *Determination of the Precipitate*

The Al-Si binary phase diagram, which shows the relationship of the binary system and the corresponding phase transitions are presented in Figure 34. Alpha, $\alpha(s)$, and beta, $\beta(s)$, are aluminum or silicon rich single-phase regions with different crystal orientations. The eutectic can be observed at certain composition and temperature with the representative lamellar structure with alternating α and β phases. According to the Al-Si phase diagram, the eutectic composition and temperature are specified as Al-12.2Si and 577 ℃, respectively. Along the vertical line on the eutectic composition, a direct transformation from the liquid phase to solid α and β phases can be observed as the temperature decreases. Other valuable information such as liquidus, solidus, or solvus can also be found in this phase diagram.

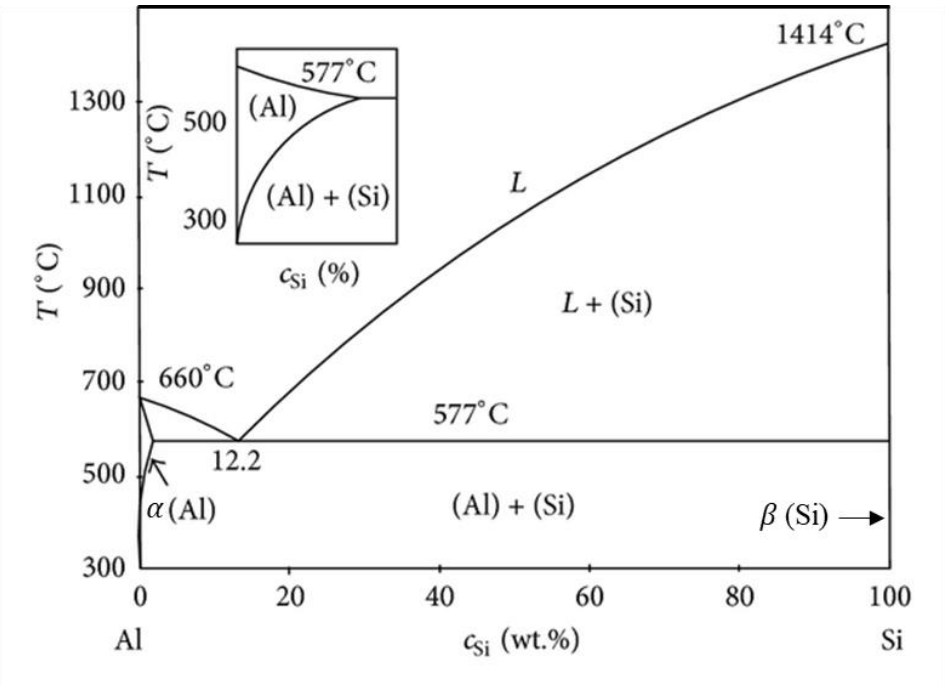

Figure 34: Binary phase diagram of Al-Si with eutectic composition of 12.2 wt% Si [108]

The phase diagram indicated the possibility of eutectic formation. Therefore, the EDX analysis was performed to identify the precipitates found in the grains of the test specimens illustrated in Figure 27 - Figure 33. To provide a direct comparison, an example of the eutectic lamellar structure of the casted AlSi10Mg is presented in Figure 35a. Unlike the casted AlSi10Mg, the test specimen fabricated in the current study revealed segregated silicon particles from the matrix (See Figure 35b). The same EDX results were observed in other test conditions, which indicates that the precipitates found in the optical

micrographs are mainly composed of silicon. The formation of the eutectic phase, therefore, was not reported from any of the test specimens in this study.

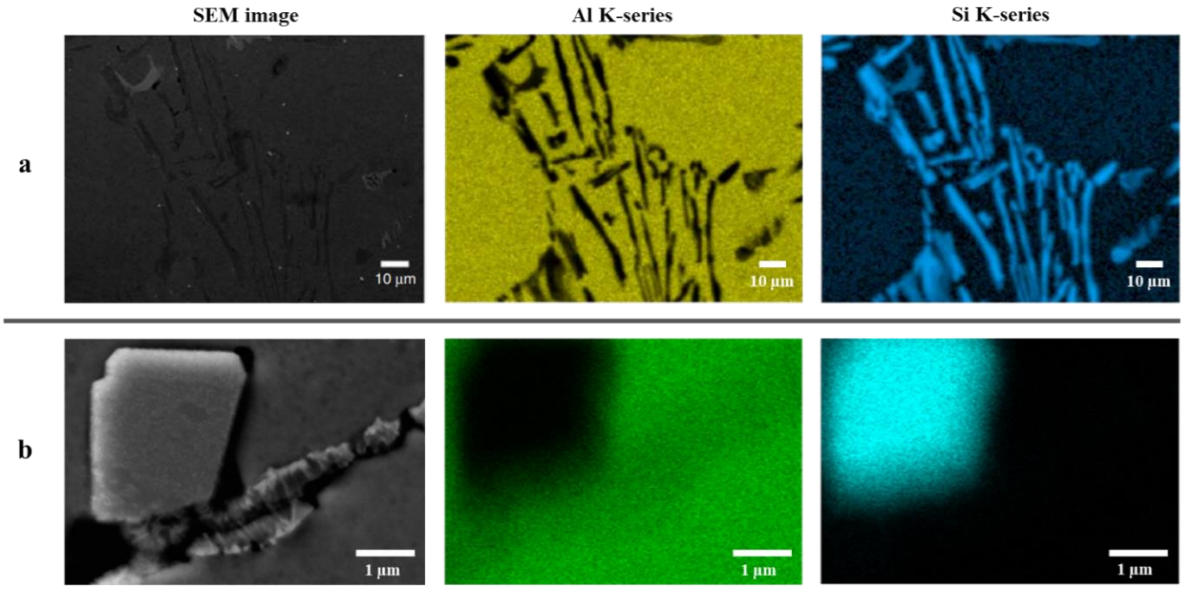

Figure 35: SEM-EDX elemental mapping images of a) casted AlSi10Mg showing the eutectic lamellar structure [109], b) binder jetted AlSi10Mg test specimen fabricated with copper oxide illustrating the segregated silicon particle from the matrix

5.4.2 *Microstructure Study of the Specimen Fabricated with the Binding Agent*

The sintered microstructure and composition of the specimen fabricated with the PAA were analyzed through performing the SEM-EDX study. This specimen was selected to be used as a reference sample since it demonstrated no contribution to the powder composition after the de-binding cycle. The secondary electron SEM image and EDX spectrum are shown in Figure 36. An undisrupted oxide film dominated the grain boundaries and hindered the sintering process [110], resulting in a lower sintered density (87.7%). A small section of the oxide film disruption was also noticed in the areas where the sintering was promoted. However, the oxide film was not completely disrupted which caused a weak sintering bond between the particles. On these grain boundaries, a trace amount of magnesium, titanium, and copper was analyzed. The representing results are illustrated in Figure 36 as Spectrum 2 and Spectrum 10. These metals (Mg, Ti, and Cu) are identified in Ellingham's diagram (See Appendix) to have a relatively high affinity to form the metal oxide. This may indicate the formation of different metal oxides along the grain boundaries instead of forming the spinel phase ($MgAl_2O_4$). As mentioned in Section 2.4.1, magnesium is a conventional sintering method used to facilitate the sintering of the aluminum powders coated with the oxide layer. This is completed by forming the spinel phase at the metal-oxide interface which allows the disruption of the passivating surface layers. Consequently, to achieve a higher density, the formation of the spinel phase is preferred. Hence, the EDX elemental analysis was performed to identify the chemical compositions on these grain boundaries.

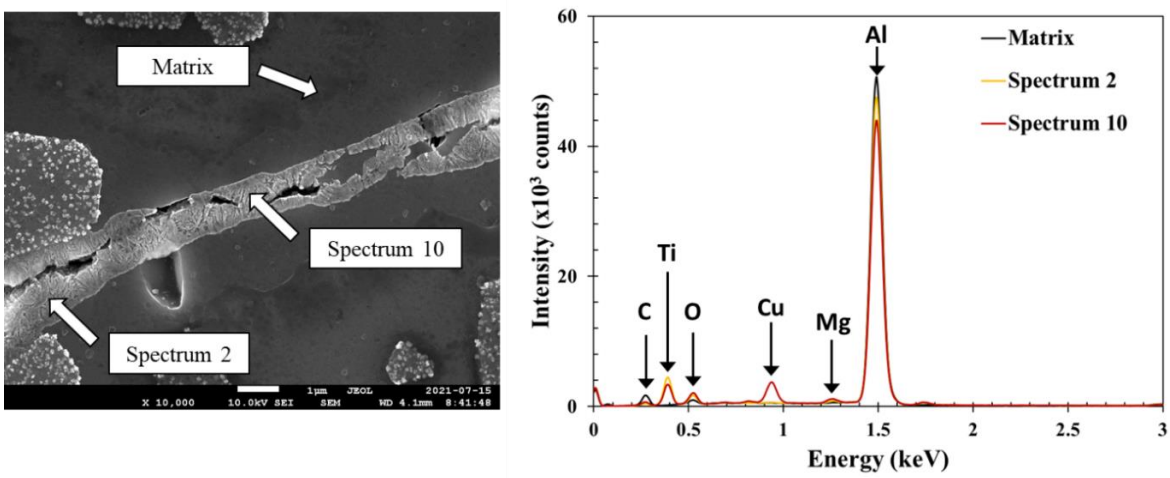

Figure 36: High-resolution SEM micrograph showing the sintered microstructure and the corresponding EDX spectrum of AlSi10Mg specimen fabricated with the PAA

The elemental analysis presented in Figure 37 displayed a possibility of other metal oxides on the grain boundaries. The spinel phase was also visible, but it was observed to be more concentrated in the inner end of the oxide film. This result implies that using the magnesium as a sole sintering mechanism is not an effective sintering mechanism for binder jetted AlSi10Mg. To understand the microstructural differences in the specimens that achieved higher sintered densities, the samples fabricated with the metallic and oxide nanoparticles, and the copper MOD ink were also investigated using the SEM and EDX.

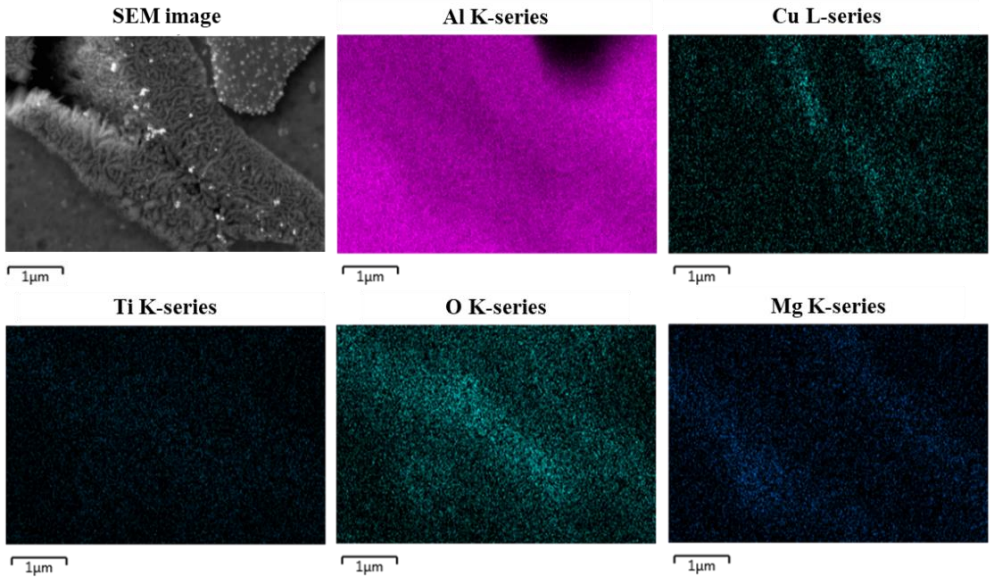

Figure 37: EDX elemental mapping images of AlSi10Mg specimen fabricated with the PAA

5.4.3 *Microstructure Study of the Specimens Fabricated with Nanoparticle Dispersions*

The first observed specimen was the sample built with the copper oxide nanoparticle dispersion that achieved a sintered density of 99.6%. The grain boundary microstructure and the corresponding EDX spectrum analysis are presented in Figure 38. Compared to the reference material, more disruptions of the oxide film were reported. However, there was still a notable amount of oxide film left undisturbed and prohibited further sintering. The EDX spectrum on these grain boundaries again showed the possibility of other metal oxide formations. The EDX analysis was followed to better understand the differences between the reference material and the nanoparticle-assisted specimen in their ability to break the oxide film.

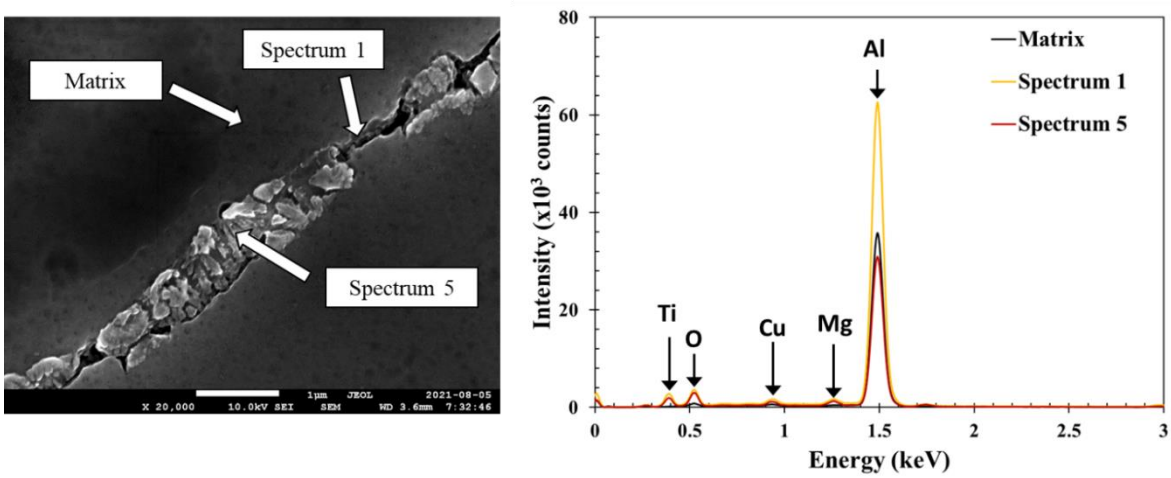

Figure 38:High-resolution SEM micrograph showing the sintered microstructure and the corresponding EDX spectrum of the AlSi10Mg specimen fabricated with the copper oxide nanoparticle dispersion

A similar pattern to the reference material of having the scattered titanium and copper particles was noticed as displayed in Figure 39. However, a substantial amount of spinel phase was observed along the outer end of the grain boundaries. Based on this result, it can be believed that the active formation of the spinel phase has helped in achieving higher densification. Although the sintering was not complete, it was evident that the integration of the copper oxide nanoparticle assisted in engaging the magnesium to be more actively involved with disrupting the passivating surface layer.

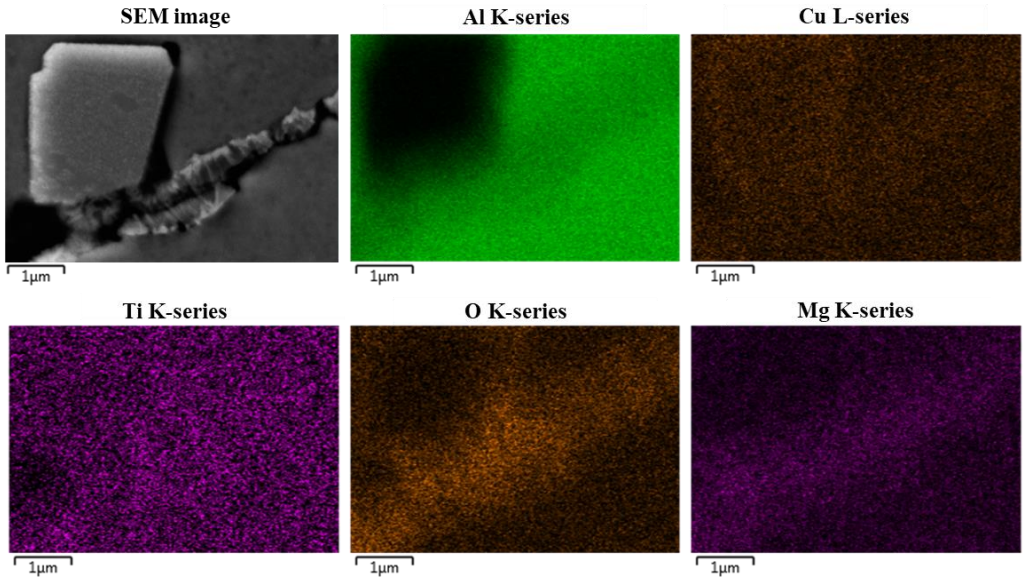

Figure 39: EDX elemental mapping images of AlSi10Mg fabricated with the copper oxide nanoparticle dispersion

The sample constructed with the aluminum oxide which demonstrated the densification of 99.1% was also studied. The observations are illustrated in Figure 40, where the sintering of the oxide films with neighboring particles was presented. Unlike other specimens, the integration of aluminum oxide merged the oxide films together instead of disrupting the layer. This explains the high densification as it removed the gap between the particles through bonding with its neighboring oxide film. It is important to understand that this could raise concern since the oxide film in-between the particles will increase the brittleness and may cause mechanical failure.

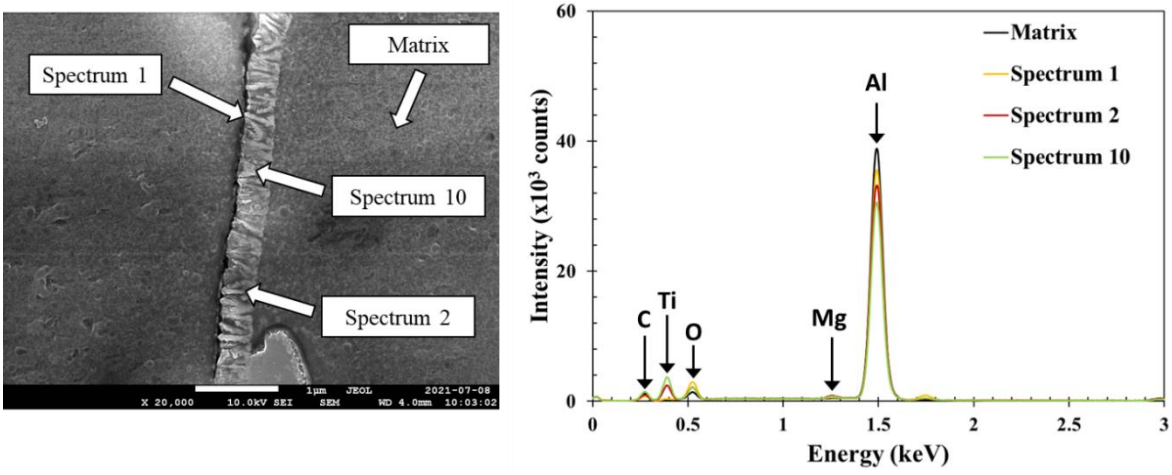

Figure 40: High-resolution SEM micrograph showing the sintered microstructure and the corresponding EDX spectrum of AlSi10Mg specimen fabricated with the aluminum oxide nanoparticle dispersion

The composition of the combined oxide film was analyzed in Figure 41. As illustrated, the undisturbed spinel phase along the grain boundary was observed. This result can also be interpreted as that the passivating films have blocked the aluminum particles from forming the sintering bond with other aluminum particles. Therefore, based on this analysis, the aluminum oxide can be concluded as an incompatible sintering agent for AlSi10Mg.

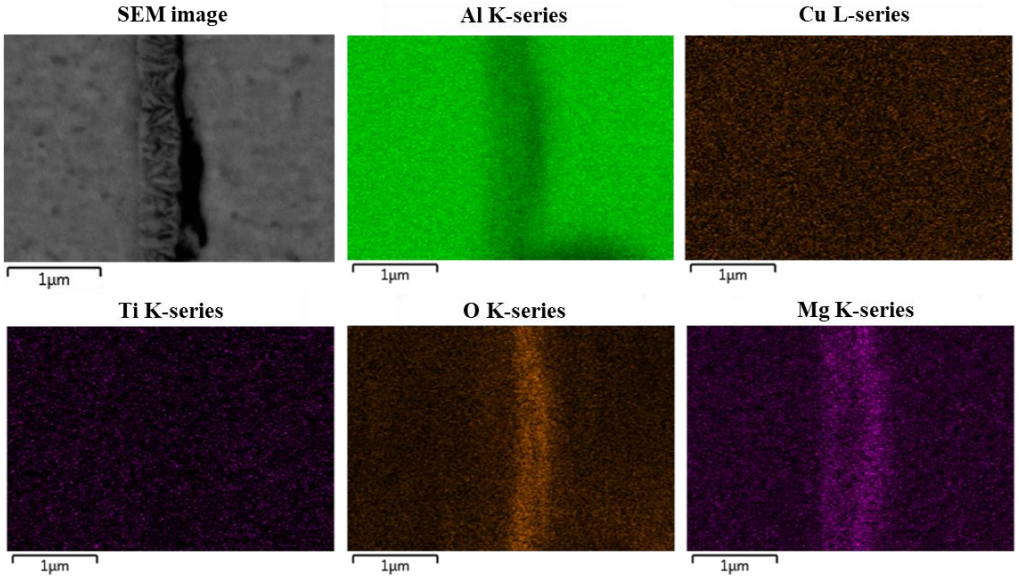

Figure 41: EDX elemental mapping images of AlSi10Mg fabricated with the aluminum oxide nanoparticle dispersion

The SEM-EDX results of the tested sample with the copper nanoparticle are shown in Figure 42. The obtained sintered microstructure displayed different constructions in contrast to the other test conditions. A completely disturbed oxide film was replaced with the reorganized structure of particle agglomerates. This reconstructed structure also has a considerably narrower thickness compared to the oxide films of the reference material or other test specimens. The EDX spectrum detected a significant amount of copper on the particles that present a brighter color (See spectrum 1). Moreover, some other particles that are mainly composed of magnesium, titanium, and oxygen were also observed. It can be believed that this reconstruction of the grain boundary had helped in opening the channels for aluminum particles to diffuse into the neighboring particles. The resulting density and the microstructure of the grain boundary already suggest that the copper nanoparticle is a highly compatible sintering agent for AlSi10Mg to promote the desired sintering behavior. However, the EDX elemental analysis was conducted for a better understanding of the correlation between the construction change of the grain boundary and the rapid increase in the copper compositions.

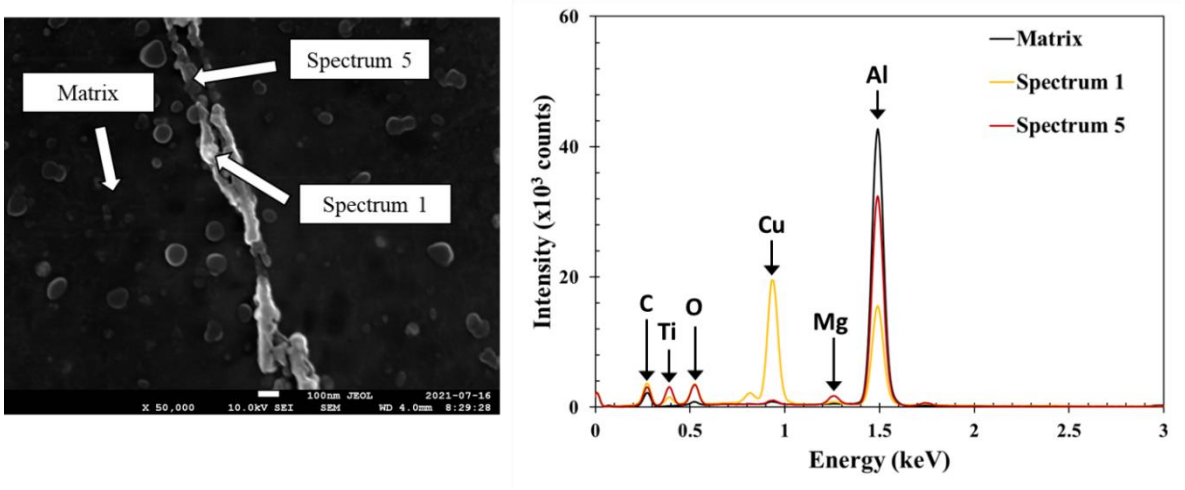

Figure 42: High-resolution SEM micrograph showing the sintered microstructure and the corresponding EDX spectrum of AlSi10Mg specimen fabricated with the copper nanoparticle dispersion

The EDX elemental images presented in Figure 43 illustrate a localized copper along the reconstructed grain boundary. This is a contradicting result compared to the other specimens where the copper particles were observed in a more scattered pattern. A substantial amount of oxygen was also found to be concentrated in the area where the copper particles were obtained. This observation indicates that the added copper nanoparticles were successful in disrupting the oxide films on the aluminum particles and formed the metal oxide to reach a more stable state. The detected spinel phase was less significant to the copper, which again suggests that the copper nanoparticles played a more important role in promoting the sintering.

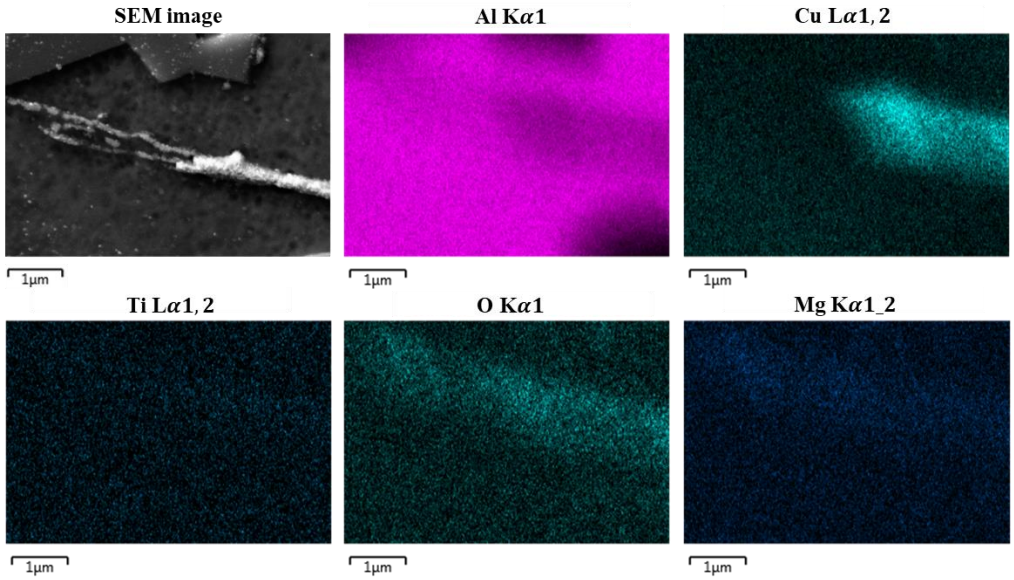

Figure 43: EDX elemental mapping images of AlSi10Mg specimen fabricated with copper nanoparticle dispersion

5.4.4 *Microstructure Study of the Specimen Fabricated with the Copper MOD Ink*

The sintered microstructure and the consequent EDX spectrum of the specimen built with the copper MOD sample are shown in Figure 44. Similar to the specimen made with the copper nanoparticle dispersion, the agglomerated particles substituted the grain boundary. The copper particles deposited from the particle-free MOD solution after the heat treatment clearly interfered with the oxide film and assisted in the sintering of the aluminum particles. This was possible because the deposited copper particles have a very small particle size (80 nm – 130 nm), and had a strong affinity to be in the more stable state.

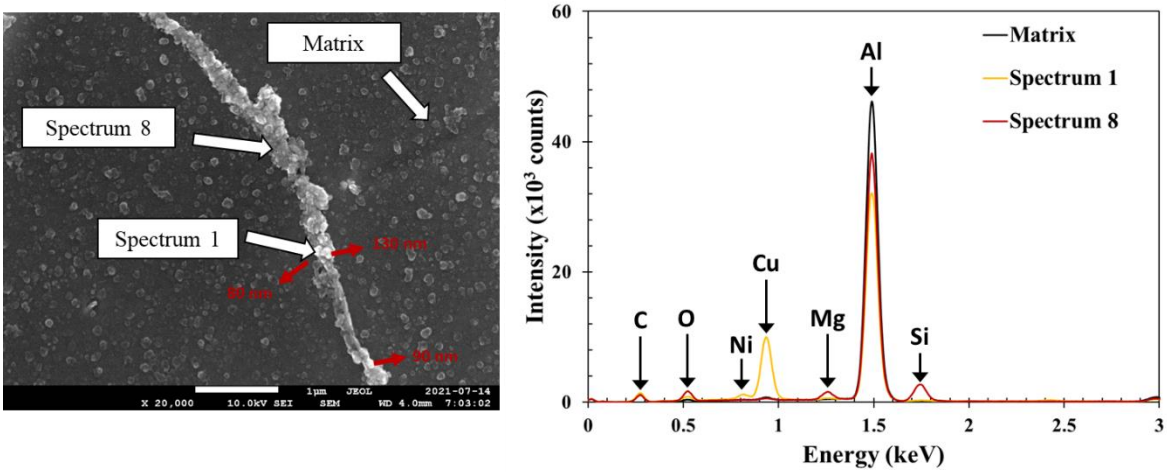

Figure 44: High-resolution SEM micrograph showing the sintered microstructure and the corresponding EDD spectrum of AlSi10Mg specimen fabricated with the copper MOD ink

In the EDX spectrum, a noticeable amount of copper was detected. However, in the EDX elemental mapping images, the formation of the spinel phase was more significant as illustrated in Figure 45. The spinel phase dominated the grain boundary with a section of areas being occupied with the copper particles. In these areas, oxygen was also found to be highly concentrated. This result suggests that the major sintering mechanism in this specimen was the formation of the spinel phase. However, the effect of the copper particles cannot be neglected as it may have opened the channel for sintering. This recommends that the integration of copper MOD ink has increased the engagement of the magnesium, which effectively allowed the diffusion of aluminum through the other particles by disturbing the oxide film. Therefore, the copper MOD ink can be concluded as another promising sintering agent that could be used to further enhance the physical property of the AlSi10Mg in the binder jetting process.

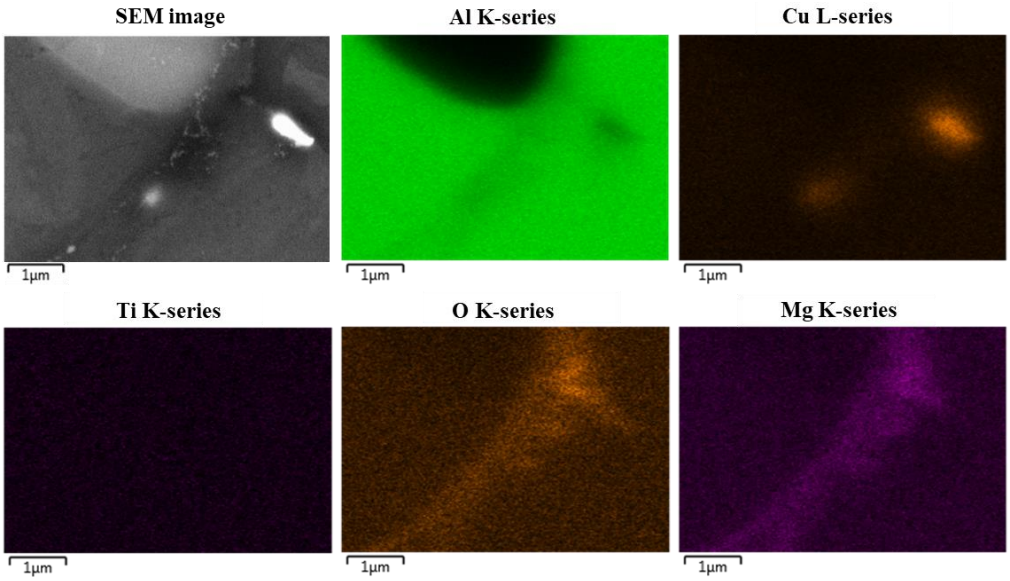

Figure 45: EDX elemental mapping images of AlSi10Mg specimen fabricated with the copper MOD ink

5.4.5 *Summary of the Microstructure Study*

The overall comparison of the EDX spectrums for the tested conditions is summarized in Figure 46 and Figure 47. The spectrums that presented high magnesium contents were plotted in Figure 46, and the spectrums with high copper contents were plotted in Figure 47. High magnesium contents were obtained with the specimens fabricated with the copper oxide and copper nanoparticle dispersions, and the samples with the copper MOD ink. This supports the analysis observed above, which emphasized the importance of the spinel phase. On the other hand, the lowest magnesium content with a relatively high oxygen composition was found with the sample constructed with aluminum oxide. This indicates the contribution of the aluminum oxide nanoparticles in sintering the oxide films which could have accumulated a subsequent amount of aluminum oxide on the grain boundaries. However, the behavior of the aluminum oxide may require further study since there was a discrepancy in the magnesium compositions between the EDX spectrum and elemental mapping images. The copper contents were compared in Figure 47 and the comparison agreed with the sintered microstructure analysis discussed in the previous chapters. The copper nanoparticle dispersions demonstrated the highest engagement of the copper particles with the oxygen, where the copper MOD ink displayed a slightly lower engagement. This signifies the particle size of the sintering agent since it appears that smaller particle size has more direct involvement in the oxide layer disruption. However, based on the porosity and microstructure analysis, both copper nanoparticle dispersion and the copper MOD ink presented effective sintering for the binder jetted AlSi10Mg.

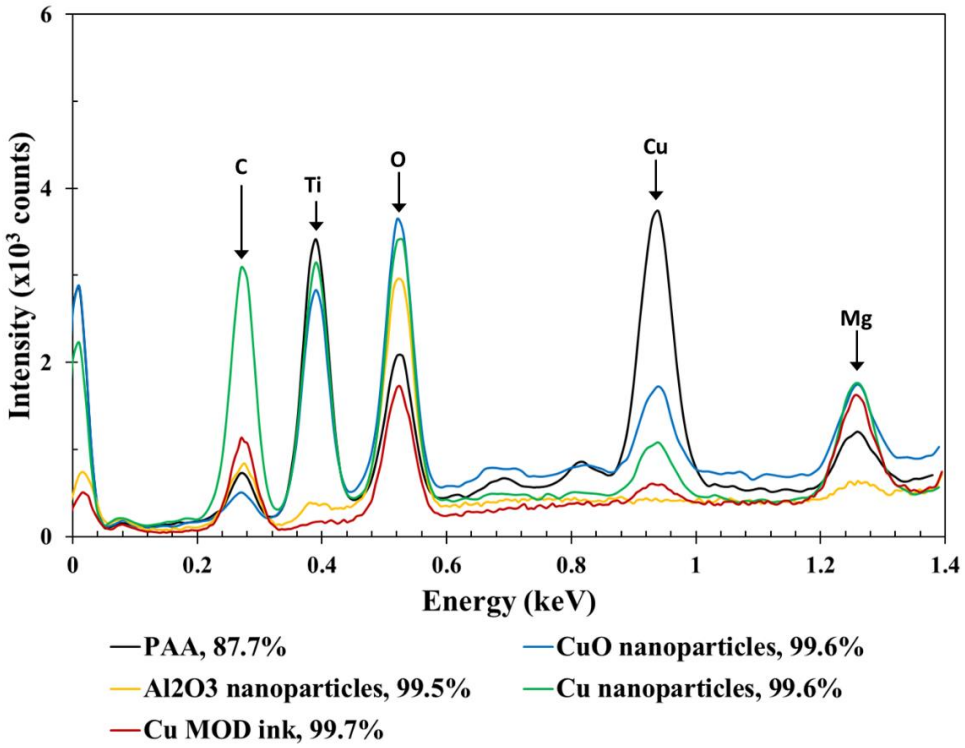

Figure 46: A comparison of the EDX spectrums of AlSi10Mg specimens presented to compare the magnesium contents

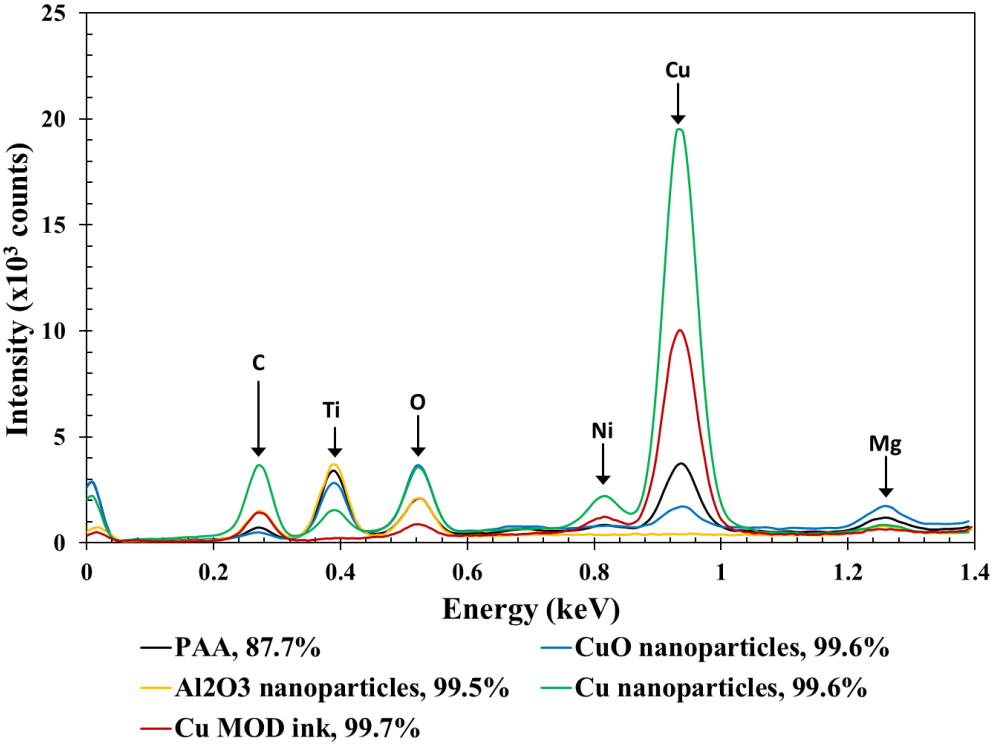

Figure 47: A comparison of the EDX spectrums of AlSi10MG specimens presented to compare the copper contents

Based on the microstructural and elemental compositional analysis, it can be concluded that copper nanoparticle dispersion and copper MOD ink were the most compatible sintering agents for processing AlSi10Mg. Hence, the cost comparison of these sintering agents is presented in Table 14. The optical micrographs and density results were utilized in deciding the compositions for the cost analysis. The copper MOD ink is suggested as a more cost-effective method that can promote the sintering of the aluminum powder.

Table 14: Cost comparison of the copper nanoparticle dispersions (5 wt%) and copper MOD ink (1 wt%)

Sintering agent	Cost [$/L of solution]
Copper nanoparticle dispersion	359.36
Copper MOD ink	164.43

6.0 Conclusion and Recommendations

The purpose of this study was to identify the 1) most compatible binding agent for the aluminum alloys that leaves minimal or no residues after the de-binding cycle, and 2) the best sintering agent that could facilitate the sintering of the aluminum alloys by disrupting the passivating oxide films. The binder compatibility study focused on discovering the residue deposition on the test specimens after the consequent de-binding cycles. In contrast, the study on the sintering agents was more focused on observing the microstructure and the elemental compositions on the grain boundaries of the test specimens. This evaluation was completed to find the alternative or additional method to be used as a sintering mechanism that can disrupt the oxide layers to allow the diffusion between the aluminum particles.

In the porosity analysis, PVP achieved the highest sintered density of 95.1%. However, the elemental analysis reported 0.008% and 0.001% of residue carbon and oxygen content even after the tailored de-binding cycle. In contrast, the PAA test specimen demonstrated a complete burnout characteristic after the de-binding cycle. Although, it only provided 87.7% of the sintered density, the complete removal of the binder was deemed more attractive. Therefore, for other test specimens that required structural support, the PAA solution was prepared to be used as a base material. In addition to the porosity analysis of the binding agents, the sintering agents were also studied to investigate their ability destruct the oxide layer. As indicated in the manuscript, all sintering agents except for the silver MOD ink achieved a near-full density.

The grain boundary microstructure analysis was followed for the selected samples to ensure the oxide layer disruption and sintering bond creation. A total of five samples were studied to investigate their

sintered microstructures with the sample fabricated by PAA used as the reference specimen. The grain boundary of the reference sample was dominated by the undisrupted oxide film with only a small section of disturbed area. As a result, sintering between the aluminum particles was not actively promoted and failed to develop a strong sintering bond. The specimen constructed with the copper oxide showed a possible disruption of the oxide film. However, a substantial amount of these passivating layers was still left undestroyed. In contrast to those two specimens, the sample made by the aluminum oxide dispersion exhibited a unique behavior. Instead of assisting the interruption of the oxide film, the addition of aluminum oxide sintered the neighboring films together. Although a high density was observed with the oxide nanoparticle specimens, a concern regarding the mechanical failure was reported.

The copper nanoparticle dispersion and copper MOD ink demonstrated a superior result in the microstructure analysis. A complete transformation of the grain boundary structure was observed. The passivating films were replaced with particle agglomerates that are composed mainly of copper, magnesium, titanium, and oxygen. This indicated the engagement of the deposited copper nanoparticle in facilitating the sintering of the selected aluminum alloy. However, a clear difference between these two sintering agents was also observed. The microstructure analysis of the copper nanoparticle dispersion indicated that the disruption was dominated by the deposited copper particles. In contrast, the result implied that the copper MOD ink was more involved in increasing the engagement of the magnesium. Nonetheless, the integration of either the copper nanoparticles or the copper MOD ink presented a very successful result. Therefore, this research is expected to benefit the BJ industry in integrating the aluminum alloys by suggesting an alternative method to disrupt the oxide layer below the melting point of the alloys.

In future studies, the mechanical properties of the tested specimens can be investigated. The mechanical characterization of these specimens can be used to better understand the microstructure result obtained in the current study. In addition, a more in-depth analysis can be performed to tailor the sintering agents to meet the required binder characteristics to be processed on the binder jetting machine. Furthermore, the printing parameters can also be studied to find the optimal printing conditions of using these sintering agents.

7.0 References

[1] D. Kim *et al*, "Streamlining the additive manufacturing digital spectrum: A systems approach," *Additive Manufacturing,* vol. 5, p. 20-30, 2014.

[2] S. Ford and M. Despeisse, "Additive manufacturing and sustainability: An exploratory study of the advantage and challenges," *Journal of Cleaner Production,* vol. 137, p. 1573-1587, 2016.

[3] D. Chen *et al*, "Direct digital manufacturing: definition, evolution, and sustainability implication," *Journal of Cleaner Production,* vol. 107, p. 615-625, 2015.

[4] M. Mani, K. W. Lyons, and S. Gupta, "Sustainability characterization for additive manufacturing," *Journal of Research of the National Institution of Standards and Technology,* vol. 119, p. 419-428, 2014.

[5] T. D. Ngo *et al.*, "Additive manufacturing (3D Printing): A review of materials, methods, applications, and challenges," *Composites Part B,* vol. 143, p. 172-196, 2018.

[6] W. Gao *et al.*, "The status, challenges, and future of additive manufacturing in engineering," *Computer-aided Design,* vol. 69, p. 65-89, 2015.

[7] G. E. Aznarte, Q. A. Jawad, and A. Cagri, "A study on material-process interaction and optimization for VAT-photopolymerization processes," *Rapid Prototyping Journal,* vol. 24, no. 9, p. 1479-1485, 2018.

[8] Y. Kim, J. Lee, and J. H. Oh, "Fabrication of fine metal patterns using an additive material extrusion process with a molten metal," *Microelectronic Engineering,* vol. 191, p. 10-15, 2018.

[9] M. Javidani *et al.*, "Additive manufacturing of AlSi10Mg alloy using direct energy deposition: microstructure and hardness characterization," *Journal of Thermal Spray Technology,* vol. 26, p. 587-597, 2017.

[10] Y. L. Yap *et al.*, "Material jetting additive manufacturing: An experimental study using designed metrological benchmark," *Precision Engineering,* vol. 50, p. 275-285, 2017.

[11] E. Malekipour and H. El-Mounayri, "Common defects and contributing parameters in powder-bed fusion AM process and their classification for online monitoring and control: a review," *International Journal of Advanced Manufacturing Technology,* vol. 95, p. 527-550, 2018.

[12] K. S. Prakash, T. Nancharaih, and V. V. Subba-Rao, "Additive manufacturing techniques in manufacturing – An overview," in *5th Materials Today,* 2018, p. 3873-3882.

[13] H. Miyanaji *et al.*, "Process development for green part printing using binder jetting additive manufacturing," *Frontiers of Mechanical Engineering,* vol. 13, no. 4, p. 504-512, 2018.

[14] A. Lores *et al.*, "A review on recent developments in binder jetting metal additive manufacturing: materials and process characteristics," *Powder Metallurgy,* vol. 62, no. 5, p. 267-296, 2019.

[15] D. Anthony *et al.*, "Fine powder recoater for three-dimensional printer," U.S Patent, *WO 2017/205289 A1*, 2017.

[16] S. Mirazababaei and S. Pasebani, "A review on binder jet additive manufacturing of 316L stainless steel," *Journal of Manufacturing and Material Processing,* vol. 3, no. 82, p. 1-36, 2019.

[17] S. Cao *et al.*, "Experimental and theoretical investigation on ultra-thin powder layering in three-dimensional printing (3DP) by a novel double-smoothing mechanism," *Journal of Manufacturing and Materials Processing Technology,* vol. 220, p. 231-242, 2015.

[18] P. k. Gokuldoss, S. Kolla, and J. Eckert, "Additive manufacturing processes: selective laser melting, electron beam melting, and binder jetting – selection guidelines," *Materials,* vol. 10, p. 672- 684, 2017.

[19] I. Rishmawi, *"Binder jetting and heat treatment of ferrous alloy,"* M.S. thesis, Mechanical & Mechatronics Engineering, University of Waterloo, Waterloo, 2019.
[20] A. Kumar *et al.,* "Effects of hot isostatic pressing on copper parts fabricated via binder jetting," *Procedia Manufacturing,* vol. 10, no. 2017, p. 935-944, 2017.
[21] T. Do, P. Kwon, and C. Shin, "Process development toward full-density stainless steel parts with binder jetting printing," *International Journal of Machine Tools & Manufacture,* vol. 121, no. 2017, p. 50-60, 2017.
[22] P. C. Lynch, C. Beniwal, and J.H. Wilck, "Integration of binder jet additive manufacturing technology into the metal casting industry," *Proceedings of the 2017 Industrial and Systems Engineering Conference,* Pennsylvania, 2017, p. 1721-1726.
[23] D. Snelling *et al.,* "Lightweight metal cellular structures fabricated via 3D printing of sand cast molds," *Advanced Engineering Materials,* vol. 17, no. 7, p. 923-932, 2015.
[24] E. Sachs *et al.,* "Production of injection molding tooling with conformal cooling channels using the three-dimensional printing process," *Polymer Engineering and Science,* vol. 40, no. 5, p. 1232-1247, 2000.
[25] S. M. Allen and E. M. Sachs, "Three-dimensional printing of metal parts for tooling and other applications," *Metal and Materials,* vol. 6, no. 6, p. 589-594, 2000.
[26] D. Hong *et al.,* "Binder-jetting 3D printing and alloy development of new biodegradable Fe-Mn-Ca/Mg alloys," *Acta Biomaterialia,* vol. 45, no. 2016, p. 375-386, 2016.
[27] A. Basalah *et al.*, "Characterizations of additive manufactured porous titanium implants," *Journal of Biomedical Materials Research B: Applied Biomaterials,* vol. 100B, no. 7, p. 1970-1979, 2012.
[28] G. T. West and J. T. Bradbury, "3D printing: a case of Zipdose technology – world's first 3d printing platform to obtain FDA approval for a pharmaceutical product," 1st ed., Germany: Wiley, 2018, p. 53-79.
[29] G. Manogharan, M. Kioko, and C. Linkous, "Binder jetting: a novel solid oxide fuel-cell fabrication process and evaluation," *The Minerals, Metals, & Materials Society,* vol. 67, no. 3, 2015.
[30] C. A. Diaz-Moreno *et al.,* "Binder jetting additive manufacturing of aluminum nitride components," *Ceramics International,* vol. 45, p. 13620-13627, 2019.
[31] M. P. Paranthaman *et al.*, "Binder jetting: A novel NdFeB bonded magnet fabrication process," *The Minerals, Metals, & Materials Society,* vol. 68, no. 7, p. 1978-1982, 2016.
[32] Y. Tang *et al.*, "Elastic modulus of 316L stainless steel lattice structure fabricated via binder jetting process," *Minerals Science and Technology,* vol. 32, no. 7, p. 648-656, 2016.
[33] E. Wheat *et al.*, "Sinter structure analysis of titanium structures fabricated via binder jetting additive manufacturing," *Materials and Design,* vol. 156, p. 167-183, 2018.
[34] E. Wheat, *"Process mapping and optimization of titanium parts made by binder jetting additive manufacturing,"* M.S. thesis, Mechanical & Mechatronics Engineering, University of Waterloo, Waterloo, 2018.
[35] Y. Bai and C. B. Williams, "Binderless jetting: Additive manufacturing of metal parts via jetting nanoparticles," Solid Freeform Fabrication 2017: *Proceedings of the 28th Annual International Solid Freeform Symposium – An Additive Manufacturing Conference,* Texas, 2017, p. 249-260.
[36] A. Mostafaei *et al.*, "Characterizing surface finish and fatigue behavior in binder-jet 3D-printed nickel-based superalloy 625," *Additive Manufacturing,* vol. 24, p. 200-209, 2018.

[37] P. Nandawana *et al.*, “Powder bed binder jet 3D printing of Inconel 718: Densification, microstructural evolution and challenges,” *Current Opinion in Solid State and Materials Science,* vol. 21, p. 207-218, 2017.
[38] A. Levy *et al.*, “Additive manufacturing of complex-shaped graded TiC/steel composites,” *Materials & Design,* vol. 118, p. 198-203, 2017.
[39] D. A. Snelling *et al.*, “Binder jetting advanced ceramics for metal-ceramic composite structures,” *International Journal of Advanced Manufacturing Technology,* vol. 92, p. 531-545, 2017.
[40] S. Banerjee and C. J. Joens, “Debinding and sintering of metal injection molding (MIM) components,” in *Handbook of Metal Injection Molding,* United Kingdom: Elsevier, 2018, ch. 7, p. 129-171.
[41] R. M. German, “Sintering practice,” in *Sintering: From Empirical Observations to Scientific Principles,* Massachusetts: Butterworth-Heinemann, 2014, ch. 15, p. 471-512.
[42] Y. Hu *et al.*, “Effects of sintering temperature and holding time on densification and mechanical properties of MIM HK30 stainless steel,” *International Journal of Metallurgy and Metal Physics,* vol. 3, no. 2, 2018.
[43] O. Coovattanachai *et al.*, “Effect of heating rate on sintered series 300 stainless steel,” *Songklanakarin Journal of Science and Technology,* vol. 32, no. 2, p. 163-167, 2010.
[44] O. Garzon *et al.*, “Post-process influence of infiltration on binder jetting technology,” *Minerals Design and Application,* vol. 65, p. 233-255, 2017.
[45] C. L. Cramer *et al.*, “Infiltration studies of additive manufacture of WC with Co using binder jetting and pressureless melt method,” *Additive Manufacturing,* vol. 28, p. 333-343, 2019.
[46] S. Banerjee and C. J. Joens, “Hot isostatic pressing (HIP) of metal injection molding (MIM),” in *Handbook of Metal Injection Molding,* United Kingdom: Elsevier, 2018, ch. 9, p. 195-202.
[47] J. Sicre-Artalejo *et al.*, “High density Inconel 718: three-dimensional printing coupled with hot isostatic pressing,” *International Journal of Powder Metallurgy,* vol. 44, no. 1, p. 35-43, 2008.
[48] R. M. German, “Infrastructure developments,” in *Sintering: From Empirical Observations to Scientific Principles,* Massachusetts: Butterworth-Heinemann, 2014, ch. 3, p. 41-69.
[49] M. N. Rahaman, “Kinetics and mechanisms of densification,” in *Sintering of Advanced Materials,* 1st ed., Z. Z. Fang, Ed. Pennsylvania: Woodhead Publishing Limited, 2010, p. 33-63.
[50] G. C. Kuczynski, “Self-diffusion in sintering of metallic particles,” *Journal of Metals,* vol. 1, no. 2, p. 169-178, 1949.
[51] M. N. Rahaman, “Kinetics and mechanisms of densification,” in *Sintering of Advanced Materials,* 1st ed., Z. Z. Fang, Ed. Pennsylvania: Woodhead Publishing Limited, 2010, p. 33-63.
[52] R. M. German, “Infrastructure developments,” in *Sintering: From Empirical Observations to Scientific Principles,* Massachusetts: Butterworth-Heinemann, 2014, ch. 3, p. 41-69.
[53] R. M. German, “Thermodynamic and kinetic treatments,” in *Sintering: From Empirical Observations to Scientific Principles,* Massachusetts: Butterworth-Heinemann, 2014, ch. 7, p. 183-226
[54] R. M. German, “Thermodynamics of sintering,” in *Sintering of Advanced Materials,* 1st ed., Z. Z. Fang, Ed. Pennsylvania: Woodhead Publishing Limited, 2010, ch. 1, p. 1-32.
[55] R. M. German, “Coarsening in sintering: Grain shape distribution, grain size distribution, and grain growth kinetics in solid-pore systems,” *Critical Reviews in Solid State and Materials Sciences,* vol. 35, no. 4, p. 263-305, 2010.

[56] J. G. R. Rockland, “The determination of the mechanism of sintering,” *Acta Metallurgica,* vol. 15, p. 277-286, 1967.
[57] S. L. Kang, “Basis of liquid phase sintering,” in *Sintering,* Massachusetts: Butterworth-Heinemann, 2005, ch. 14, p. 199-203.
[58] S. Ashley, “Steel cars face a weighty decision,” *Mechanical Engineering,* vol. 119, no. 2, p. 56-61, 1997.
[59] J. F. Flumerfelt, *“Aluminum powder metallurgy processing,”* Ph.D. thesis, Metallurgy, Iowa State University, Iowa, 1998.
[60] I. A. MacAskill *et al.*, “Effects of magnesium, tin and nitrogen on the sintering response of aluminum powder,” *Journal of Materials Processing Technology,* vol. 210, p. 2252-2260, 2010.
[61] T. B. Sercombe, “On the sintering of uncompacted, pre-alloyed Al powder alloy, *Materials Science and Engineering,* vol. 341, p. 163-168, 2003.
[62] R. N. Lumley, T. B. Sercombe, and G. B. Schaffer, “Surface oxide and the role of magnesium during the sintering of aluminum,” *Metallurgical and Materials Transactions A,* vol. 30A, p. 457-463.
[63] A. Kimura *et al.*, “Reduction mechanism of surface oxide in aluminum alloy powder containing magnesium studied by x-ray photoelectron spectroscopy using synchrotron radiation,” *Applied Physics Letters,* vol. 26, no. 30, p. 3615-3617, 1997.
[64] K. Kondoh, A. Kimura, and R. Watanabe, “Effect of Mg on sintering phenomenon of aluminum alloy powder particle,” *Powder Metallurgy,* vol. 44, no. 2, 2001.
[65] Z. Y. Liu, T. B. Sercombe, and G. B. Schaffer, “Metal injection moulding of aluminium alloy 6061 with tin,” *Materials Science & Engineering Collection,* vol. 51, no.1, p. 78 -83, 2008.
[66] T. B. Sercombe and G. B. Schaffer, “On the role of tin in the nitridation of aluminium powders,” *Scripta Materialiaa,* vol. 55, p. 323-326, 2006.
[67] J. Ni, K. Han, and M. Yu, “Development of hypereutectic AlSi alloy powder injection molding feedstocks by rheological analysis”, *Advances in Materials Science and Engineering,* vol. 2018.
[68] R. K. Enneti *et al.,* “Powder-bed formulation and compound manufacture in metal injection molding (MIM)” in *Handbook of Metal Injection Molding,* United Kingdom: Elsevier, 2018, ch. 4, p. 57-88.
[69] J. Ni, M. Yu, and K. Han, “Debinding and sintering of an injection-molded hypereutectic Al-Si alloy,” *Materials,* vol. 11, no. 5:807, 2018.
[70] V. P. Onbattuvelli *et al.,* “The effects of nanoparticle addition on binder removal from injection molded aluminum nitride,” *International Journal of Refractory Metals and Hard Materials,* vol. 36, p. 77-84, 2013.
[71] J. M. Martin and F. Castro, “Liquid phase sintering of P/M aluminum alloys: effect of processing conditions,” *Journal of Materials Processing Technology,* vol. 143-144, p. 814-821, 2003.
[72] M. Kurakula and G. S. N. K. Rao, “Pharmaceutical assessment of polyvinylpyrrolidone (PVP): As excipient from conventional to controlled delivery systems with a spotlight on COVID-19 inhibition,” *Journal of Drug Delivery Science and Technology,* vol. 60: 102046, 2020.
[73] Y. Feng *et al.*, “Effect of the addition of polyvinylpyrrolidone as a pore-former on microstructure and mechanical strength of porous alumina ceramics,” *Ceramics International,* vol. 39, no. 7, p. 7551-7556, 2013.
[74] M. Ziaee and N. B. Crane, “Binder jetting: A review of process, materials, and methods,” *Additive Manufacturing,* vol. 28, p. 781-801, 2019.

[75] S. M. Gaytan *et al.*, "Fabrication of barium titanate by binder jetting additive manufacturing technology," *Ceramics International,* vol. 41, no. 5: Part A, p. 6610-6619, 2015.
[76] D. Karlsson *et al.*, "Binder jetting of the AlCoCrFeNi alloy," *Additive Manufacturing,* vol. 27, p. 72-79, 2019.
[77] H. Miyanaji, N. Momenzadeh, and L. Yang, "Effect of printing speed on quality of printed parts in binder jetting process," *Additive Manufacturing,* vol. 20, p. 1-10, 2018.
[78] N. D. Parab *et al.*, "Real time observation of binder jetting printing process using high-speed X-ray imaging," *Scientific Reports,* vol. 9, no. 2499, 2019.
[79] C. Xiao *et al.*, "Effect of polyvinylpyrrolidone on rheology of aqueous SiC suspensions with polyethylene glycol as binder" *Colloids and Surfaces A: Physicochemical and Engineering Aspects,* vol. 368, no. 1-3, p. 53-57, 2010.
[80] V. G. Kadjji and G. V. Betageri, "Water soluble polymers for pharmaceutical applications," *Polymers,* vol. 2011, no. 3, p. 1972-2009, 2011.
[81] M. Teodorescu, M. Bercea, and S. Morariu, "Biomaterials of PVA and PVP in medical and pharmaceutical applications: Perspectives and challenges," *Biotechnology Advances,* vol. 37, no. 1, p. 109-131, 2019.
[82] S. Baklouti *et al.*, "Binder burnout and evolution of the mechanical strength of dry-pressed ceramics containing poly(vinyl alcohol)," *Journal of the European Ceramic Society,* vol. 21, no. 8, p. 1087-1092, 2001.
[83] K. J. Voorhees, S. F. Baugh, and D. N. Stevenson, "The thermal degradation of poly(ethylene glycol)/poly(vinyl alcohol) binder in alumina ceramics," *Thermochimica Acta,* vol. 274, p. 187-207, 1996.
[84] L. Gong, M. Nguyen, and E. Oh, "High polar polyacrylonitrile as a potential binder for negative electrodes in lithium ion batteries," *Electrochemistry Communications,* vol. 29, p. 45-47, 2013.
[85] J. K. Papp *et al.*, "Poly(vinylidene fluoride) (PVDF) binder degradation in Li-O_2 batteries: A consideration for the characterization of lithium superoxide," *The Journal of Physical Chemistry Letters,* vol. 8, no. 6, p. 1169-1174, 2017.
[86] B. Qu *et al.*, "Stabilization of metal (II) oxides on the nanoscale," *Materials Research Letters,* vol. 8, no. 1, p. 41-47, 2020.
[87] T. Yokoyama *et al.*, "Basic properties and measuring methods of nanoparticles," in *Nanoparticle Technology Handbook,* United Kingdom: Elsevier, 2007, ch. 1, p. 5-10.
[88] L. Xu *et al.*, "Stability and reactivity: Positive and negative aspects for nanoparticle processing," *Chemical Reviews,* vol. 118, p. 3209-3250, 2018.
[89] N. B. Crane, "*Strengthening porous metal skeletons by metal deposition from a nanoparticle dispersion,*" Ph. D. thesis, Mechanical Engineering, Massachusetts Institute of Technology, Massachusetts, 2005.
[90] P. Kunchala and K. Kappagantula, "3D printing high density ceramics using binder jetting with nanoparticle densifiers," *Materials & Design,* vol. 155, no. 5, p. 443-450, 2018.
[91] Y. Bai and C. B. Williams, "The effect of inkjetted nanoparticles on metal part properties in binder jetting additive manufacturing," *Nanotechnology,* vol. 29, no. 39, 2018.
[92] Y. Bai and C. B. Williams, "Binder jetting additive manufacturing with a particle-free metal ink as a binder precursor," *Materials & Design,* vol. 147, p. 146-156, 2018.
[93] Y. Choi, K. Seong, and Y. Piao, "Metal-organic decomposition ink for printed electronics," *Advanced Materials Interfaces,* vol. 6, 2019.

[94] N. Wu *et al.*, "Generalized Gibbs free energy of confined nanoparticles," *The Global Home of Chemical Engineers (AIChE),* vol. 63, no. 10, p. 4595-4603, 2017.
[95] J. D. Byrne and J. A. Baugh, "The significance of nanoparticles in particle-induced pulmonary fibrosis," *McGill Journal of Medicine,* vol. 11, no. 1, p. 43-50, 2008.
[96] L. Xu *et al.*, "Stability and reactivity: porosity and negative aspects for nanoparticle processing," *Chemical Reviews, vol. 118, no. 7, p. 3209-3250, 2018.*
[97] M. Vaseem, G. Mckerricher, and A. Shamim, "Robust design of a particle-free silver-organo-complex ink with high conductivity and inkjet stability for flexible electronics," *Applied Materials and Interfaces,* vol. 8, no. 1, p. 177-186, 2016.
[98] X. Nie, H. Wang, and J. Zou, "Inkjet printing of silver citrate conductive ink on PET substrate," *Applied Surface Science,* vol. 261, p. 554-560, 2012.
[99] K. Black *et al.*, "Silver ink formulations for sinter-free printing of conductive films," *Scientific Reports,* vol. 6, 2016.
[100] A. L. Dearden *et al.,* "A low curing temperature silver ink for use in ink-jet printing and subsequent production of conductive tracks," *Macromolecular Rapid Communications,* vol. 26, p. 315-318, 2005.
[101] Y. Dong *et al.*, "Facile synthesis of high silver content MOD ink by using silver oxalate precursor for inkjet printing applications," *Thin Solid Films,* vol. 589, p. 381-387, 2015.
[102] Y. Yong *et al.*, "Effect of decomposition and organic residues on resistivity of copper films fabricated via low-temperature sintering of complex particle mixed dispersions," *Scientific Reports,* vol. 7, 2017.
[103] D. Shin *et al.*, "A self-reducible and alcohol-soluble copper-based metal-organic decomposition ink for printed electronics," *American Chemical Society,* vol. 6, no. 5, p. 3312-3319, 2014.
[104] Y. Choi and S. Hong, "Effect of the amine concentration on phase evolution and densification in printed films using Cu (II) complex ink," *American Chemical Society,* vol. 31, no. 29, p. 8101-8110, 2015.
[105] S. Tam, K. Fung, and M. Ng, "High copper loading metal organic decomposition paste for printed electronics," *Journal of Materials Science,* vol. 52, p. 5617-5625, 2017.
[106] *836 Series oxygen/nitrogen/hydrogen by inert gas fusion*, LECO Corporation, 2018.
[107] *CS844 Carbon/sulfur by combustion,* LECO Corporation, 2019.
[108] M. B. Djurdjevic *et al.*, "Calculation of liquidus temperature for aluminum and magnesium alloys applying method of equivalency," *Simulation and Optimization in Materials Technology,* vol. 2013.
[109] G. Sander *et al.,* "Corrosion of additively manufactured alloys: A review", *NACE International Corrosion,* vol. 74, No. 12, p. 1318-1350, 2018.
[110] S. H. Huo *et al.*, "Aluminum powder metallurgy," in *Fundamentals of Aluminum Metallurgy*, United Kingdom: Woodhead Publishing Limited, 2011, ch. 21, p. 655-701.

Appendix

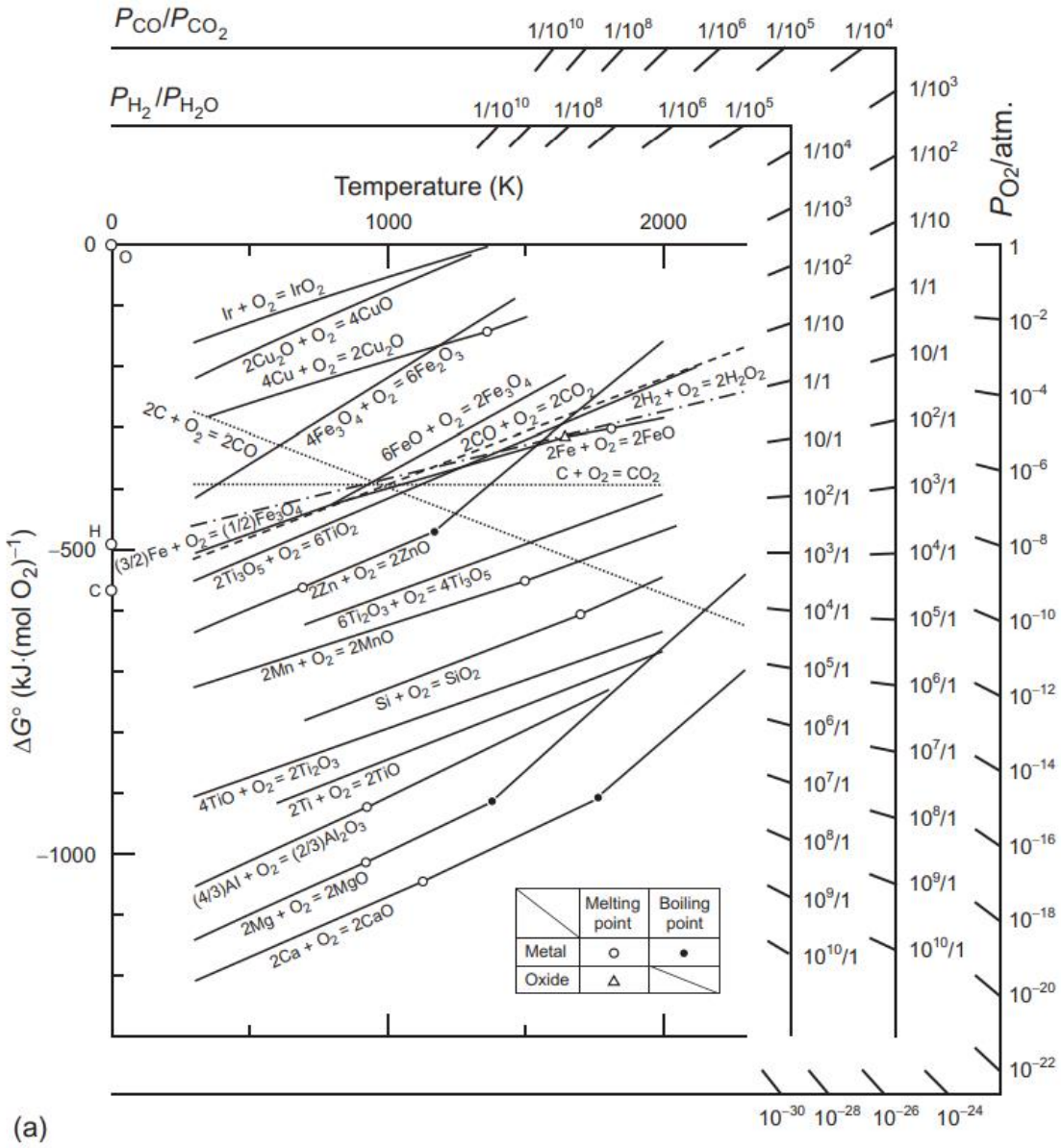

Figure 3.3.1 Ellingham diagram for some oxides; Richardson nomographic scales are included: (a) Al, Ca, Cu, Fe, Ir, Mg, Mn, Si, Ti, and Zn.